Journal of Building Engineering 99 (2025) 111564

Contents lists available at ScienceDirect

Journal of Building Engineering

journal homepage: www.elsevier.com/locate/jobe

Self-healing of biochar-cement composites with crystalline admixture exposed to sulphate solution and simulated seawater

Xuqun Lin [a], Quang Dieu Nguyen [a,*], Arnaud Castel [a,**], Zhizhong Deng [a], Wengui Li [b], Vivian W.Y. Tam [c]

[a] School of Civil and Environmental Engineering, University of Technology Sydney, NSW, 2007, Australia
[b] Centre for Infrastructure Engineering and Safety, School of Civil and Environmental Engineering, University of New South Wales, NSW, 2052, Australia
[c] Westen Sydney University, School of Engineering, Design of Built Environments, NSW, 2751, Australia

ARTICLE INFO

Keywords:
Crystalline admixtures
Biochar
Self-healing product
Seawater
Sulphates
XRD
Image analysis
SEM-EDS
FTIR
Cracking energy

ABSTRACT

Although many studies considered crystalline admixtures (CA) as the self-healing agent, only limited studies investigated the potential effects of aggressive ions on the self-healing performance of marine structures. Furthermore, there is an increasing trend to use SCMs to improve concrete resilience while lowering carbon footprint. This study investigated the effects of CA and sustainable waste wood biochar (WWB) on the self-healing of cement pastes exposed to simulated seawater or 5 % sodium sulphate solution. Three-point loading was used to initiate the cracks while keeping the cracked samples unseparated. The healing rate was investigated using optical microscopy and binary image processing. The self-healing products characterisation was conducted using Scanned Electron Microscopy equipped with Energy dispersive X-ray spectroscopy (SEM-EDS), X-ray diffraction (XRD), Thermogravimetric analysis (TG), and Fourier-transform Infrared Spectroscopy (FTIR). Cracks were completely healed after 42 days for CA-based samples when exposing to wet/dry cycles in seawater (SWWD) and sulphate solution (SWD). EDS, XRD and TG results confirmed the formation of calcite as the main healing products, while a small portion of brucite was observed in healing products for SWWD. FTIR spectra further confirmed the formation of C-S-H gel and AFt in healing productions exposed to SWWD and SWD. Although WWB addition did not improve healing performance of WWB-cement composites, it led to a relatively complex cracking path, providing more nucleation sites for the self-healing process.

1. Introduction

The concept of self-healing concrete is attracting increasing attention [1,2], being a promising approach to heal the cracks without additional labour maintenance. Although cementitious composites have the inherent capacity to self-heal cracks due to their continuous hydration [3,4], the crack-repairing efficiency is limited [5,6]. It is already reported that the addition of self-healing agents, such as superabsorbent polymers [7,8], hollow glass fibres [9,10], bacterial capsulation [11–14], and crystalline admixtures (CA) [15–20] improves the self-healing performance of the cementitious composites. Among these crack-repairing strategies, the

* Corresponding author.
** Corresponding author.
E-mail addresses: quangdieu.nguyen@uts.edu.au (Q.D. Nguyen), arnaud.castel@uts.edu.au (A. Castel).

https://doi.org/10.1016/j.jobe.2024.111564
Received 21 October 2024; Received in revised form 27 November 2024; Accepted 9 December 2024
Available online 11 December 2024

application of CA as self-healing agent in cementitious composites in both non-aggressive (air exposure or water curing) and aggressive environments (freeze/thaw cycles, chloride solution, or sulphate solution) has attracted raising interests. In terms of self-healing mechanism of CA, several studies [15,21,22] reported that CA powder stimulated different crystalline deposits healing the crack of pre-cracked cementitious samples. Similarly, many studies [2,23,24] found that calcium-based precipitations were induced to improve the healing performance of CA-based cementitious composites.

In terms of non-aggressive environment, Guenca et al. [25] found that adding CA in pre-cracked mortar samples led to complete crack healing at the first cracking-healing cycle (3-month curing), and 70 % crack closure at second cracking-healing cycle (6-month curing). Zhang et al. [15] observed that 1.5 wt% CA significantly improved the healing efficiency of the cement mortar at 28 days. Likewise, curing samples in steam at a temperature of 80° for 3 days, Xue et al. [26] reported that white deposits were induced by CA healing the crack surface and blocking pores. In a study by Azarsa et al. [27], they mentioned that 2 wt% CA could not only reduce the permeability of the cementitious samples, but also improve the healing performance of cracked concrete samples at 28 days. Similarly, Guenca et al. [28] reported that CA addition led to completed crack closure for CA-cement concrete after 6 months. Lauch et al. [29] stated that CA promoted the formation of calcite sealing the cracks in CA-cement concrete samples subjected to wet/dry cycles for 3 months. However, Tsampali and Stefanidou et al. [30] observed that, at 28 days, CA-cement samples exposed to water immersion had better healing performance when compared to CA-samples cured in wet/dry cycles. They mentioned that CA addition led to improved healing rate and lower water absorption. Ferrara et al. [31] observed that CA promoted the healing capacity of CA-cement mortar at 28 days and completely healed the crack after 6 month of exposure. Li et al. [32] reported that significant differences in self-healing performances were observed for cementitious mortar with and without CA. They concluded that CA stimulated the formation of calcite repairing the crack surface. Overall, the addition of CA improved the self-healing capacity of both cementitious pastes and mortars subjected to non-aggressive exposure conditions.

Regarding the self-healing efficiency of CA-cement composites subjected to aggressive curing environments, Aspiotis et al. [33] found that CA healed the cracks of CA-cement samples cured in freeze/thaw cycle (FTC) after 6 months. Ferrara et al. [20] observed needle-like self-healing products in the cracked surface by SEM image after exposing samples in FTC. Xue et al. [23] observed that the crack closure rate of samples cured in chloride solution was higher than that of samples cured in water after 30 days. They mentioned that the formation of ettringite accelerating the crack repairing rate. Similarly, other studies [24,34] reported improved healing efficiency of MgO-cement composites in seawater using CA, where brucite formed in the cracks. However, based on the aforementioned literatures, the investigations of self-healing behaviours of CA-cement composites in aggressive curing environments are limited.

Due to the progress of urbanisation, coastal infrastructures including long cross-sea bridges, coastal roads, and built residential and commercial buildings near the ocean are increasingly being built [35,36]. However, concrete structures are vulnerable in such harshly combined conditions of salts crystallisation and tidal motion [12]. Cracks inevitably occur to reduce the serviceability of the structures [37]. Aggressive ions, such as chlorides, sulphates, and magnesium ions would penetrate into the cementitious matrix leading to further strength deterioration and crack development. Recently, several studies reported that using different supplementary cementitious materials (SCMs), such as slag [38,39] or biochar [40,41], could improve the chloride resistance of samples with SCMs in marine environments, prolonging the serviceability of marine structures. Lin et al. [42] reported that up to 5 wt% biochar could be used to replace General Purpose cement (GPC) without lowering the mechanical properties and the chloride resistance of biochar-cement composites. However, there is no current literature reporting self-healing behaviour of biochar-cement composites in marine environment, limiting broader applications of biochar in coastal concrete structures.

The primary purpose of this study was to investigate the self-healing behaviour of biochar-cement composites in marine environment with the presence of CA, including healing rate monitoring and self-healing product characterisations. Simulated seawater and sodium sulphate solution were used as aggressive curing environments for both permanent solution immersion and wet/dry cycles. The healing behaviour of paste specimens was monitored using optical microscopy and binary image processing. The Interfacial-transitional zone (ITZ) in the healed zone was analysed using Scanned Electron Microscopy equipped with Energy dispersive X-ray spectroscopy (SEM-EDS). Furthermore, the compositions of the healing products was characterised using X-ray diffraction (XRD), Thermogravimetric analysis (TG), and Fourier-transform Infrared Spectroscopy (FTIR). The novelty of this study is to provide more insights into the potential effects of aggressive ions, such as chloride, magnesium, and sulphates, on the healing behaviour of biochar-cement composites, highlighting the role of CA and biochar in the self-healing process of cementitious composites in the aggressive environments.

Table 1
Pastes mix designs.

Mix designs	GPC	Water	Crystalline admixture	WWB	Superplasticizer	Water/binder ratio	Flow (mm)
CO	1	0.35	–	–	–	0.35	228 ± 1.5
CCA	1	0.35	0.01		–	0.35	227 ± 1.4
CWB	1	0.35	0.01	0.05	0.012	0.35	226 ± 2.2
WBC	1	0.35	–	0.05	0.012	0.35	227 ± 1.8

Note: GPC refers to general purpose cement, and WWB denotes blended waste wood biochar.

2. Methodology

2.1. Raw materials and sample preparation

Commercial GPC by Boral Australia, PENETRON Admix CA by PENETRON Australia, and blended waste wood biochar (WWB) by Green Man Char Australia was used. Raw material information, including chemical compositions, particle size distribution, and SEM morphologies, of CA and WWB was reported in our previous study [43]. Based on the XRF results in the previous study [43], PENETRON Admix CA mainly contained 49.24 % CaO, 41.15 % SiO_2, and 9.15 % Na_2O. The mix designs of all paste prism samples are provided in Table 1. CO donates the control group, and CCA refers to cementitious paste samples with 1 wt% CA. WBC group is the samples with 5 wt% WWB replacing GPC, and CWB is named after adding 1 wt% CA in BC samples. It should be noted that Superplasticizer (Sikament® Eco WR, Sika Australia) was added to maintain comparable flows between samples with and without WWB (Table 1.) The potential effects of CA on the self-healing behaviour of cementitious composites subjected to seawater and sulphate solutions could be compared using CO and CCA group. CO group, CWB group, and WBC group are used to access the potential effects of WWB addition on the healing behaviours of biochar-cement composites in aggressive environments.

It should be noted that all powders were mixed in a 5L Hobart Mixer with a speed of 16 rpm for 3 min to achieve uniform distribution of solid constituents. A 24-rpm speed mixing was then used to mix all powders with ½ water content for 2 min, and the mixing process was continued for another 3 min after adding the other ½ water content. To avoid loss of binder materials, fresh mixture on the mixer's bowl was shovelled down followed by a 16-rpm speed mixing for 2 min. After that, 1-min vibration was conducted for uniform compaction of all cementitious samples after casting the fresh cementitious mixture into the moulds with dimensions of 40 × 40 × 160 mm. Notably, 56 prisms were prepared for the time-dependent self-healing monitoring and self-healing products collection as shown in Table 2. Plastic foil was immediately used to cover all fresh samples till demoulding after 24-h curing. Finally, all specimens were stored in a controlled chamber with 95 ± 5 % relative humidity and 23 ± 2 °C temperature until formal investigation.

2.2. Solution preparation and exposure conditions

For simulating a marine exposure condition, several studies [44,45] used simulated seawater complying with ASTM D1141-98 [46], being close to natural seawater. As a result, this study adopted this simulated seawater as the marine exposure environment to investigate the self-healing performance of biochar-cement samples with and without CA. Commercially available sodium chloride, magnesium chloride, anhydrous sodium sulphate, calcium chloride, and potassium chloride (Rowe Scientific, Australia) were added into deionised water to prepare the simulated seawater. Table 3 summarises the concentration of the different salts in the simulated seawater. As per ASTM D1141-98, 0.1N NaOH solution was added into the simulated seawater to adjust pH at 8.2 using a digital pH metre. 5 % Na_2SO_4 solution was prepared using anhydrous sodium sulphate and deionised water.

Many studies [2,16,27] mentioned that limited healing capacity was observed in air exposure. Thus, air exposure was not considered in this study. Two exposure conditions were adopted (Table 4), including permanent immersion and wet/dry cycle (WD). For WD, samples were immersed in solution for 3 days, and dried in a conditioned storage room with 23 ± 2 °C temperature and relative humidity of 50 ± 5 % for 4 days. Based on self-healing regime adopted in previous studies [23,47], all plastic containers were stored in the conditioned room during the curing period up to 42 days. It should be noted that a weekly renew of two solutions was conducted to maintain the pH values for the first month, and thereafter biweekly till 42 days.

2.3. Self-healing monitoring

2.3.1. Artificial crack

An AGX50 bending machine was employed to initiate the load-induced crack in all samples (Fig. 1a). As shown in Fig. 1b, three lines were drawn at 30 mm, 80 mm, and 130 mm from one end of the samples to achieve a centred position by aligning the three lines with the 2 roller supports and the loading point accordingly. The loading rate was 0.1 mm/min. Loading was stopped after a crack occurred. It should be noted that although a cracking line penetrated into the cementitious prism, the prism remained unseparated rather than breaking into two portions (Fig. 1c).

Table 2
Sample casting details.

Experimental method	Mix design	Number of samples	Condition
Time-dependent self-healing monitoring	CO	8	Cracked
	CCA	8	Cracked
	CWB	8	Cracked
	WBC	8	Cracked
Collections of self-healing product	CO	6	Sliced
	CCA	6	Sliced
	CWB	6	Sliced
	WBC	6	Sliced

Table 3
Compounds of simulated seawater as per ASTM D1141-98.

Compounds	NaCl	$MgCl_2$	Na_2SO_4	$CaCl_2$	KCl
Concentration (g/L)	24.53	5.20	4.09	1.16	0.695

Table 4
Exposure conditions for self-healing evaluation.

Solution	Exposure conditions
Simulated seawater	Permanent immersion; Wet/dry cycle (SWWD)
Sodium Sulphate solution	Permanent immersion; Wet/dry cycle (SWD)

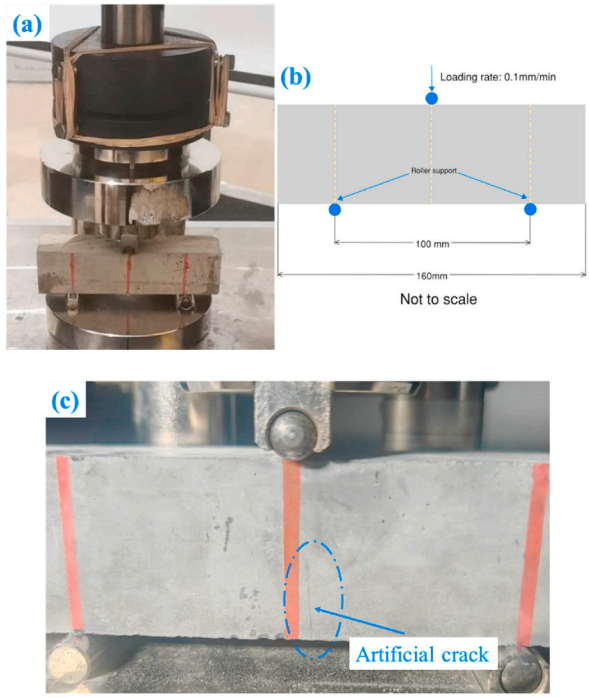

Fig. 1. Artificial crack initiation: (a) 3-point bending programme; (b) Loading position and loading rate; (c) Unbroken CO sample with a cracking line.

2.3.2. *Time-dependent healing process*

This study combined two methods to investigate the self-healing performance of the different pastes, including optical microscopy analysis and binary processing at 0 day, 28 days and 42 days respectively. After a crack was created, a Carl Zeiss Axiotech Vario 100 HD equipped with Eakins 48 MP FHD Camera was immediately used to measure the crack width for all samples (Fig. 2a). It should be noted that 5 points were measured per pre-cracked sample. The average initial crack widths for all pre-cracked samples were summarised in Table 5. As depicted in Fig. 2b–a typical crack width of 121.27 μm was measured using a 10x-magnification lens in Carl Zeiss Axiotech camera.

In terms of binary image processing, as shown in Fig. 2c, images were taken before formal solution immersion. A greyscale image was converted mitigating potential colour variances (Fig. 2d). By using ImageJ, the background of the greyscale image was removed to keep only the crack line for the binary processing (Fig. 2e). After that, a binary function in ImageJ was employed to convert the greyscale image into a black-white image with a dimension of 787 × 2841 pixel (Fig. 2f). Some studies [48,49] indicated that a reduction in the white area would be the evidence of crack-healing progress in the binary image processing. Importantly, the Scale function in ImageJ was utilised to keep all binary-processed image within the same dimension of 787 × 2841 pixel. The white area in binary image of a CO sample at 0 day was calculated as 35173 pixels using ImageJ (Fig. 2g), while the crack healing rate (φ_{CHR}) was calculated using Eq. (1):

$$\varphi_{CHR} = \frac{WA_t}{WA_i} \times 100\% \quad (1)$$

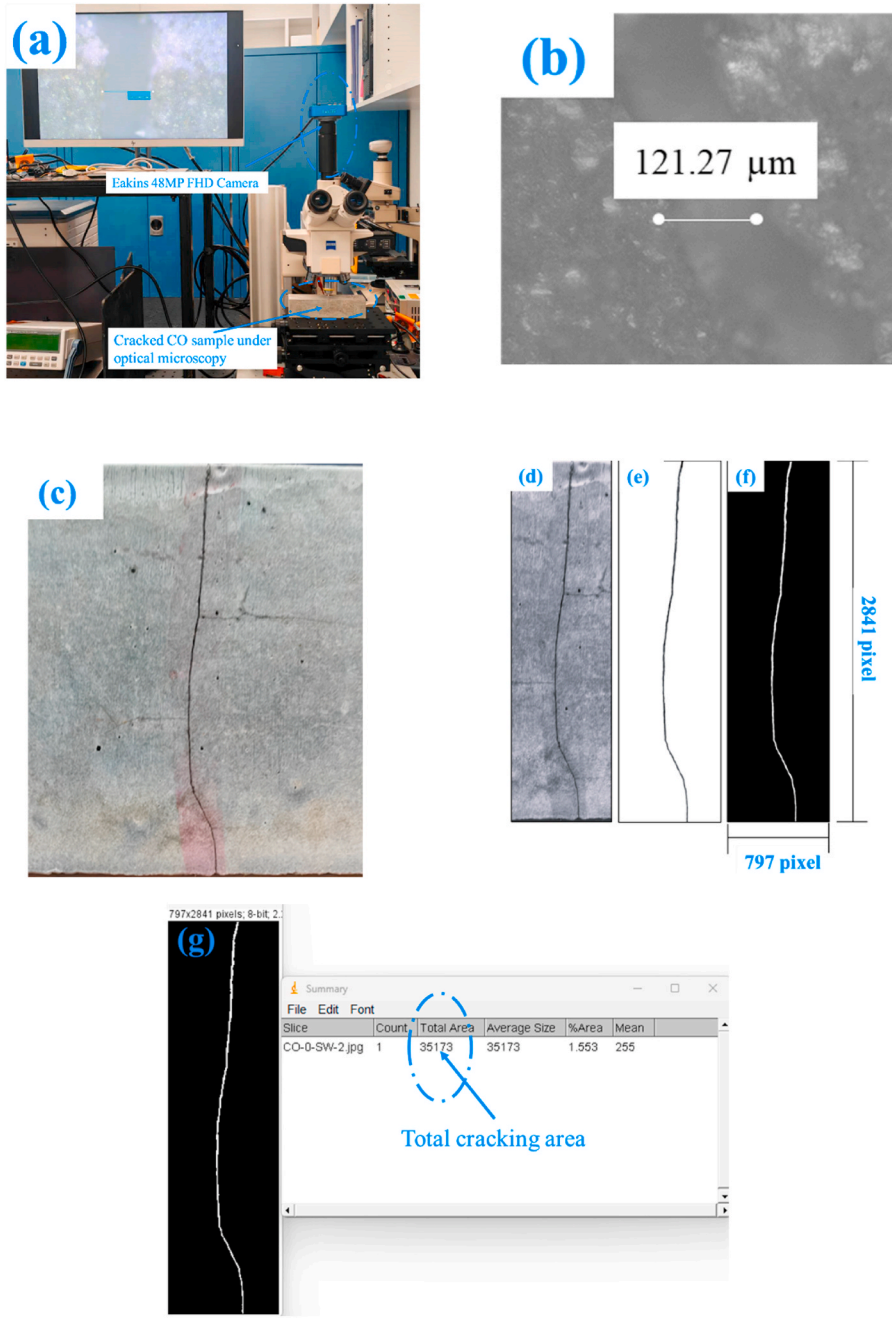

Fig. 2. Time-dependent monitoring programme: (a) Optical microscopy observation; (b) Crack width of a CO sample; (c) Original photo of cracked CO sample; (d) Greyscale image of cracked sample; (e) Crack observation with background-subtract process; (f) Binary process; (g) cracking area by pixel calculation.

Where φ_{CHR} is the time-dependent healing rate (%), WA_i is the initial cracking area in white pixels, and WA_t refers to the final cracking area at t days in white pixels.

2.3.3. Scanned Electron Microscopy (SEM-EDS)

Self-healing products were analysed using a Zeiss Supra 55VP SEM equipped with Energy dispersive X-ray spectroscopy (SEM-EDS). A healed sample was coated with epoxy resin protecting the healing products during slicing-induced vibration (Fig. 3a). A Struers Labotom-15 cutting equipment was utilised to cut the healed portion from the prism (Fig. 3b). Then, precise cutting was performed using a Struers Secotom-20 precise cutting machine (Fig. 3c), where the line was 5 mm above the specimen's base with crack opening.

Table 5
Average initial cracking widths.

Exposure solutions	Mix design	Average cracking widths (mm)
Sodium sulphate solution	CO	123.85 ± 5.5
	CCA	129.43 ± 9.5
	CWB	148.56 ± 4.9
	WBC	134.37 ± 7.2
Simulated seawater	CO	121.73 ± 6.5
	CCA	127.62 ± 4.3
	CWB	147.15 ± 3.8
	WBC	137.85 ± 4.8

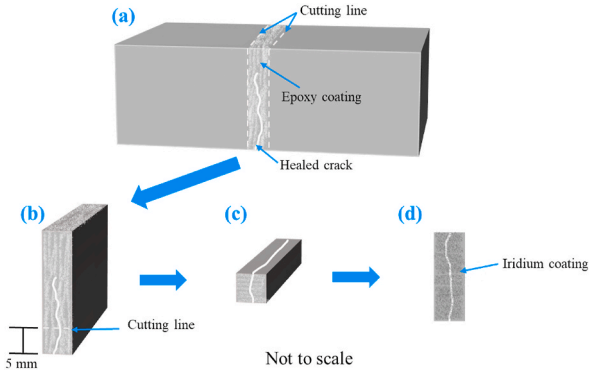

Fig. 3. SEM sample preparation: (a) cracking surface coated with Epoxy resin; (b) Sliced part with healed crack; (c) precise cutting; (d) Iridium coating.

It should be noted that all sliced portions were marked and stored in an oven at 45 °C for 1 week. Iridium coating was used to coat the healed surface using a Leica EM ACE600 coater (Fig. 3d). SEM-EDS analysis was then conducted with a voltage of 10 kV and a working distance of 7 mm–7.8 mm. As shown in Fig. 3d, the SEM-EDS observations were performed on the surface containing the whole cracking line, being parallel to the specimen's base.

2.4. Self-healing product analysis

Additional samples (Table 2) were sliced into 10-mm portions using a Struers Labotom-15 cutting equipment. A rubber band was used to tie the sliced portions (Fig. 4a). The exposure method followed WD regime as stated in Section 2.2, including simulated seawater and 5 % Na_2SO_4. After 42 days, tied portions were opened and washed using deionised water to remove salt crystallisation on the healing products, and these portions were immersed in an isopropanol solution of 99.9 % purity for 1 day before storing them in an oven at 45 °C for 2 days. Then, self-healing products on each site were carefully scratched (Fig. 4b). Finally, the self-healing products were characterised using X-Ray Diffraction (XRD), Thermogravimetric analysis (TG), and Fourier-transform Infrared Spectroscopy (FTIR).

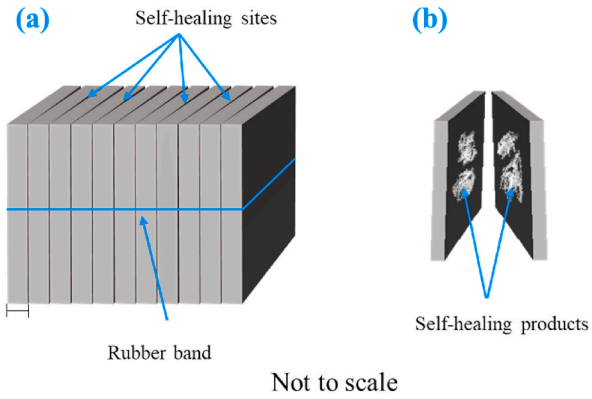

Fig. 4. Self-healing products collection: (a) Self-healing site initiation; (b) Self-healing product scratching.

XRD analysis was performed using a Bruker D8 Discover diffractometer (Cu Kα, λ = 1.54 Å). In particular, the diffraction angle (2θ) was set in the range of 5° to 70° using a sample spinner, measured at the scanning step of 0.02°. Bruker Topas equipped with Crystallography Open Database was then used to characterise the mineralogy of the self-healing products.

A NETZSCH STA 449 Jupiter was employed to analyse the decomposition process of self-healing products at different thermal events. Up to 30 mm powder was weighted using an alumina crucible, and a 30-min standby was set with nitrogen environment at 40 °C. After that, the final temperature was set at 1000 °C with healing rate of 10 °C/min. The nitrogen gas flow remained 50 ml/min during the TG analysis [44,50]. TG and Derivative TG were utilised to calculate the mass loss of C-S-H gel, portlandite, and calcite in percentage.

FTIR analysis was conducted using a Nicolet 6700 FTIR spectrometer with a spectra ranging from 450 to 4000 cm^{-1} wavenumber. The resolution was set at 8 cm^{-1}.

3. Results

3.1. Optical microscopy analysis

Fig. 5 presents the crack closure of the different samples using the optical microscopy up to 42 days. In this study, different curing conditions were considered, including permanent sulphate immersion (SI), permanent seawater immersion (SWI), wet/dry cycle in sulphate solution (SWD), and wet/dry cycle in seawater (SWWD), as shown in Fig. 5a to d respectively. It worth noting that samples cured in SWD and SWWD showed complete crack closure after 42 days, while samples without CA addition had limited crack repairing.

In terms of SI and SWI, white deposits were observed on the surface of all samples with CA addition. The presence of water activated the special chemicals in CA, promoting the formation of white crystal deposits on the cracked surface. In sulphate solution, healing products could be found at both sides of the cracking line. It should be note that due to a relatively thin cracking width (120.81 μm) in CCA group (Fig. 5a6), there was a connection between healing products from both sides after 42 days. No apparent healing product connections were found in CWB sample with a cracking width of 151.56 μm (Fig. 5a7). Likewise, exposed to seawater for 42 days, healing products formed on both sides of the cracking line in CCA group (Fig. 5b6) and CWB group (Fig. 5b7). However, due to the absence of CA in CO and WBC group, negligible amount of healing products was observed.

For SWD (Fig. 5c) and SWWD (Fig. 5d), complete crack healing was observed in CCA and CWB group after 42 days, being consistent with other studies [24,51]. For samples without CA, only limited white deposits were found in CO and WBC group in SWD after 42 days. This phenomenon may be only due to the inherently continuous hydration of unhydrated cement grains. Similarly, white deposits were formed on both sides of the cracking surface in CO and WBC group in SWWD at 42 days. Notably, without CA addition, there were not significant differences in crack closure for CO and WBC samples in permanent solution immersion and wet/dry cycle. For CCA group, cracking lines with width of 138.81 μm and 135.89 μm were completely healed when subjected to SWD and SWWD respectively. It is worth noting that due to the presence of 5 wt% WWB, wider cracking widths of 152.36 μm and 141.56 μm were completely healed (Fig. 5c7 and Fig. 5d7).

By comparing SI and SWD, and SWI and SWWD, samples exposed to wet/dry cycle showed more effective crack closure. When moving samples from the different solutions to the ambient environment, the presence of carbon dioxide would promote the healing efficiency, having a good agreement with Tittelboom [52]. Some studies [24,34,51] confirmed the formation of calcite in healing products in cracked specimens exposed to marine environments or simulated seawater. As a result, WD could be conservatively considered as the best exposure regime in promoting the healing performance of samples with CA addition. The presences of water and carbon dioxide led to the complete crack closure after 42 days. The characterisation of healing products would be discussed in Section 3.4.

3.2. Binary analysis

3.2.1. Wet/dry cycles in seawater

Binary process was used to further classify the healing rate of samples exposed to SWWD up to 42 days (Fig. 6). It should be noted that all binary images were scaled to the same dimensions of 797 * 2841 pixels to compare the cracking area reduction of the different pastes in the WD regime. The time-dependent cracking area reductions of all samples are summarised in Table 6.

Fig. 7 depicts different healing efficiency of the pre-cracked samples in SWWD. As shown in Table 6, using 5 wt% WWB to replace cement led to relatively higher cracking area at 0 day, being 49697 and 41168 pixels for CWB and WBC sample respectively. Meanwhile, when compared to the flat cracking path of the CO (Fig. 6a) and CCA group (Fig. 6b), relatively tortuous cracking paths were observed in CWB (Fig. 6c) and WBC group (Fig. 6d). Some studies [53,54] explained that instead of a direct penetration into the cementitious matrix, cracking energy was absorbed by biochar particles, disrupting the cracking development leading to a more complex path. At 28 days, the remaining cracking area was 28922, 5321, 8939, and 31370 pixels for CO, CCA, CWB, and WBC respectively (Table 6). It should be noted that the addition of CA promoted 86.36 % and 82.01 % cracking closure for CCA and CWB group respectively. In terms of CA-free samples, there was still 82.23 % and 76.2 % unhealed cracking area remaining for CO and WBC group. Due to the continuous cement hydration, limited amount of healing products was observed in the middle of the CO and WBC samples (Fig. 6a4 and Fig. 6d4).

At 42 days, only limited self-healing was observed in CA-free samples, since 62.68 % and 58.96 % cracking area remained unhealed for CO and WBC groups. However, 5 wt% WWB seemed to improve the healing efficiency, where it promoted 41.04 % crack closure at 42 days. In terms of CA-cement composites, 100 % crack healing rate was found in CCA and CWB group at 42 days (Fig. 7). Similar

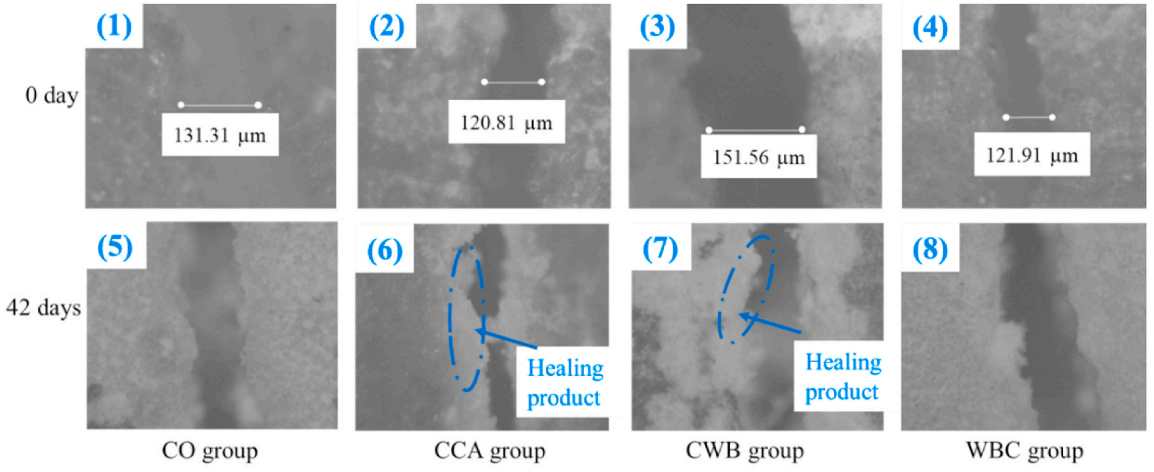
(1)
(2)
(3)
(4)
0 day
131.31 μm
120.81 μm
151.56 μm
121.91 μm
(5)
(6)
(7)
(8)
42 days
Healing product
Healing product
CO group
CCA group
CWB group
WBC group

(a)

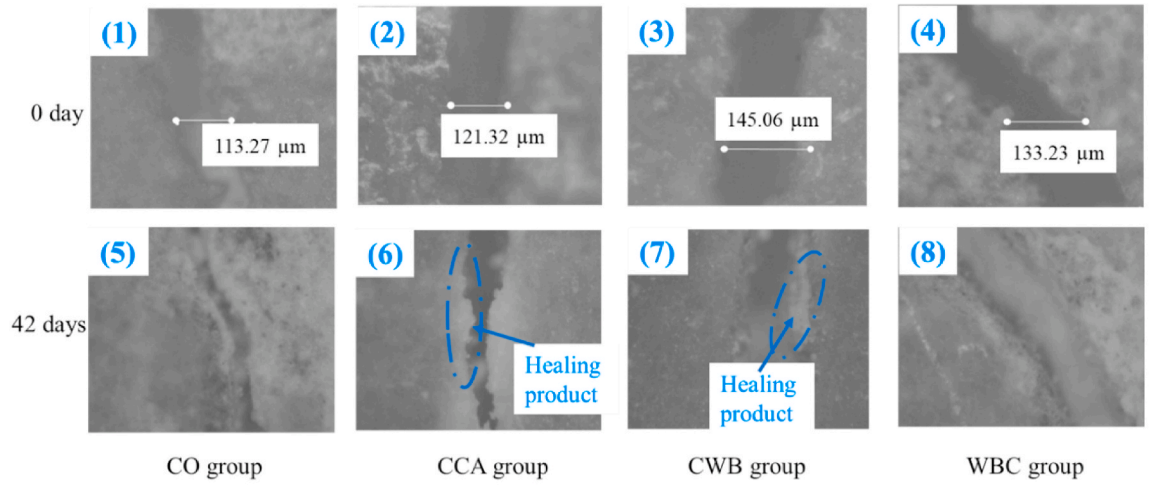
(1)
(2)
(3)
(4)
0 day
113.27 μm
121.32 μm
145.06 μm
133.23 μm
(5)
(6)
(7)
(8)
42 days
Healing product
Healing product
CO group
CCA group
CWB group
WBC group

(b)

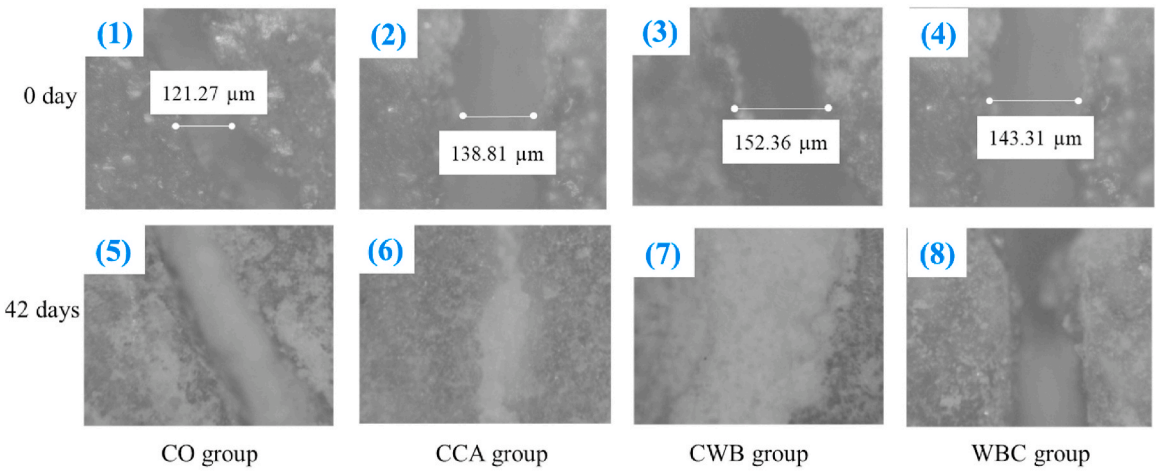
(1)
(2)
(3)
(4)
0 day
121.27 μm
138.81 μm
152.36 μm
143.31 μm
(5)
(6)
(7)
(8)
42 days
CO group
CCA group
CWB group
WBC group

(c)

Fig. 5. Optical microscopy monitoring of cracking closure using Carl Zeiss Axiotech microscopy with 10x magnification: (a) Permanent sulphate immersion; (b) Permanent seawater immersion; (c) Wet/dry cycle in sulphate solution; (d) Wet/dry cycle in seawater.
(Note: CO group means the control group, CCA group is samples with 1 wt% CA only, CWB group refers to samples with 1 wt% CA and 5 wt% WWB, and WBC group is samples with 5 wt% WWB only.

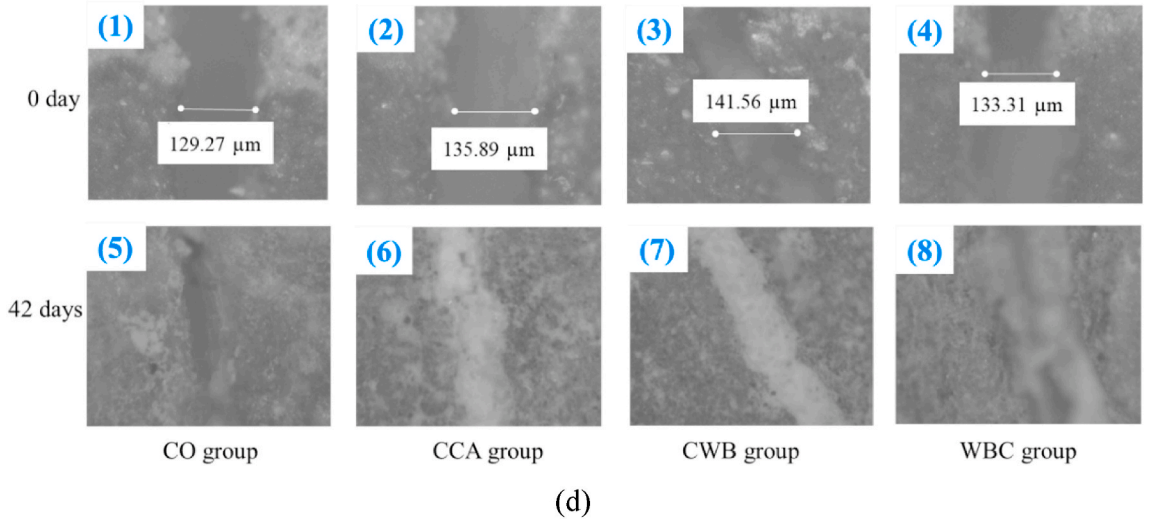

Fig. 5. (*continued*).

findings were reported by several studies [55,56]. Exposing samples in marine environment, Liu et al. [57] observed larger amount of calcium and magnesium ions in the healing products than those in the nearby cementitious matrix, promoting the formation of calcite and small amount of magnesium-based product filling the crack. It was observed that the cracking line was completely healed by white deposit in CCA and CWB group at 42 days (Fig. 6b7 and Fig. 6c7).

Overall, curing samples in seawater, CCA and CWB samples showed 86.36 % and 82.01 % crack healing respectively at 28 days and complete crack closure at 42 days. For CA-free samples, limited healing behaviour was observed.

3.2.2. *Wet/dry cycles in sulphate*

Fig. 8 shows the time-dependent healing behaviours of samples cured in SWD up to 42 days. Similar to samples cured in SWWD, binary images in SWD were scaled to 797 * 2841 pixels, so the healing performances of different pastes could be compared up to 42 days. The time-dependent healing rates of the four groups exposed to SWD are depicted in Table 7. It should be noted that the area of air bubble in CWB was not included in the area calculation using binary process.

CWB sample had the highest cracking area (45592 pixels) at 0 day, due to relatively complex cracking path when compared to WWB-free samples. After 4 WD cycles in the sulphate solution, partial crack closure was observed for all groups. The cracking area reduction trend in SWD is presented in Fig. 9. At 28 days, the cracking areas of CCA and CWB were significantly reduced due to the formation of white deposits in the cracks (Fig. 8b4 and Fig. 8c4), being 84.2 % and 88.49 % reduction respectively. In terms of CA-free samples, 30.87 % and 22.14 % cracking area reduction were observed for CO and WBC group respectively. Although white deposits randomly distributed along the cracking surface in CO and WBC group (Fig. 8a4 and Fig. 8d4), the lack of CA powder limited the healing efficiency at 28 days.

At 42 days, the cracking line in CCA was completely healed (Fig. 8b7). However, due to the presence of a large air bubble, the crack in CWB was healed by 99.61 % (Fig. 8c7). It is worth noting that without any air bubble in CWB sample, the crack would be completely repaired. As a result, 100 % crack closure was achieved in both CCA and CWB group after 6 SWD cycles. For samples without CA addition, 42.82 % and 35.51 % healing rate was found in CO and WBC group respectively, indicating the effectiveness of CA promoting the healing performance in sulphate solution.

Overall, CA addition significantly improved the healing performance of the CA-cement composites at 28 days and totally healed the cracks after 42 days. However, there was no significant differences in healing performance of samples cured in SWWD and SWD conditions. As a result, SEM-EDS was used to investigate the compositions of healing products in samples cured in SWWD and SWD.

3.3. *SEM-EDS analysis*

As shown in Fig. 10, samples for SEM-EDS analysis were dried and coated with iridium. It should be noted that the coated surface was sliced perpendicularly to the cracking depth (Fig. 3), where a healed cracking line was observed in a CCA sample (Fig. 10a). Similar strategies were applied to samples cured in SWD and SWWD conditions, allowing to compare the differences in the chemical compositions of the healing products.

The SEM-EDS analysis of a CCA sample exposed to SWWD is given in Fig. 11. Using 400x magnification, different healing products

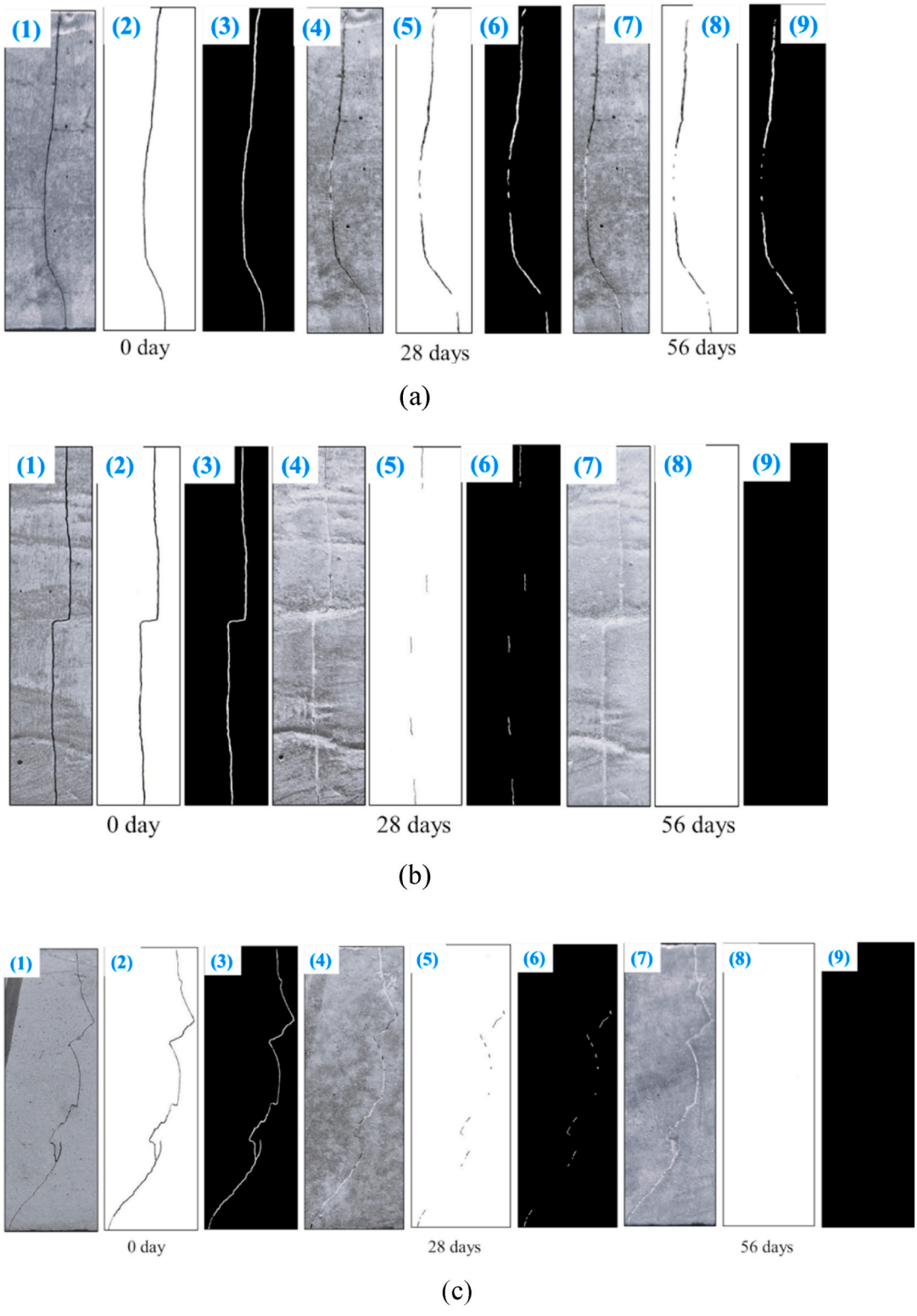

Fig. 6. Binary image in SWWD: (a) CO group; (b) CCA group; (c) CWB group; (d) WBC group.

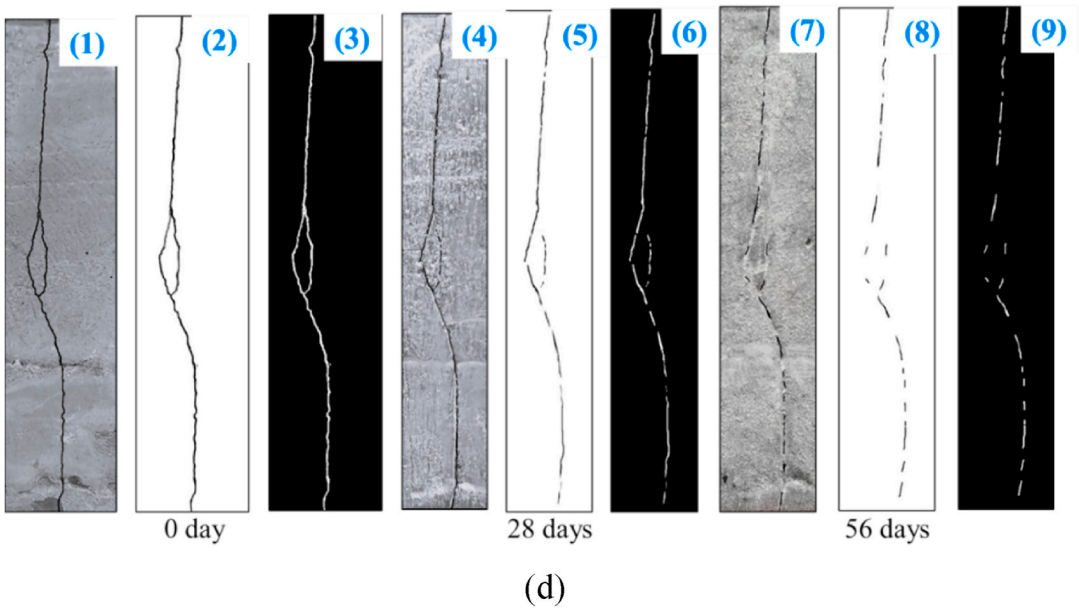

Fig. 6. (*continued*).

Table 6
Healing efficiency of samples cured in SWWD.

Mix design	Exposure age	Total image area (pixels)	Remaining crack area (pixels)	Remaining cracking area (%)
CO	0 day	2264277	35173	100.00
	28 days	2264277	28922	82.23
	42 days	2264277	22046	62.68
CCA	0 day	2264277	39019	100.00
	28 days	2264277	5321	13.64
	42 days	2264277	0	0.00
CWB	0 day	2264277	49697	100.00
	28 days	2264277	8939	17.99
	42 days	2264277	0	0.00
WBC	0 day	2264277	41168	100.00
	28 days	2264277	31370	76.20
	42 days	2264277	24273	58.96

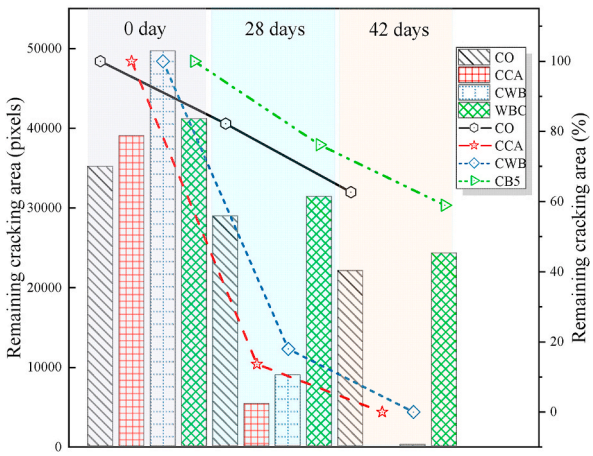

Fig. 7. Time-dependent cracking closure in seawater.

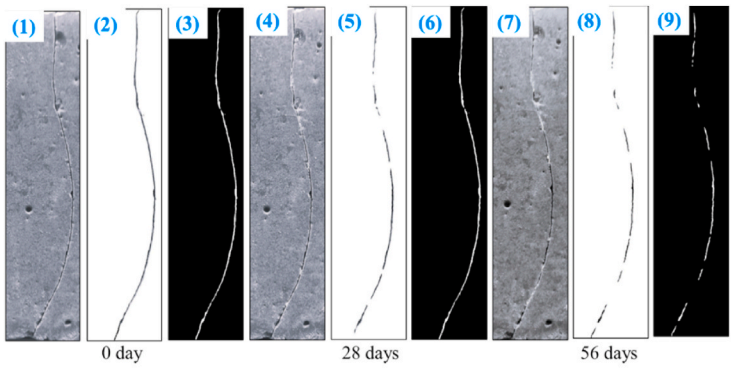

(a)

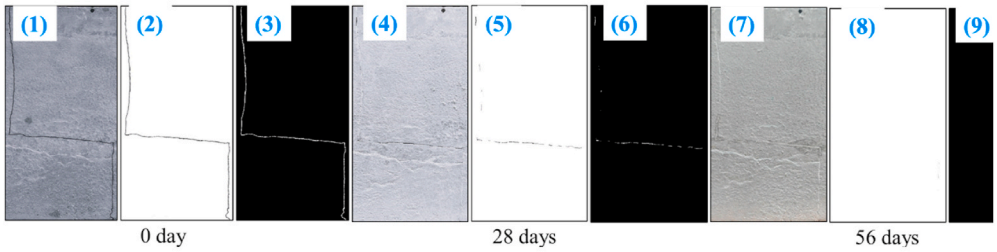

(b)

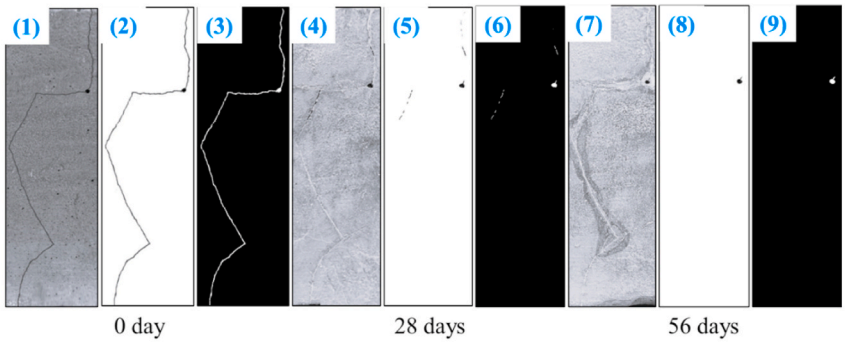

(c)

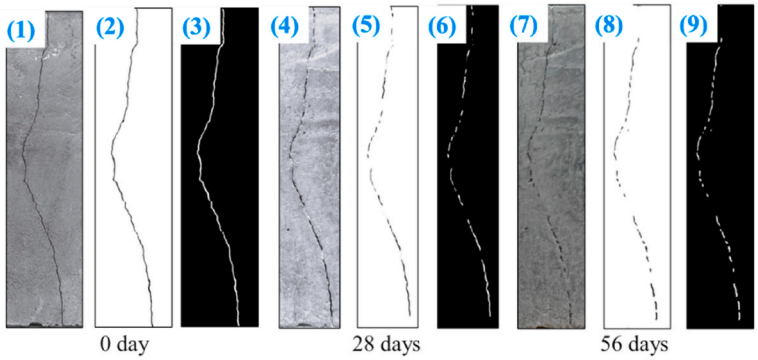

(d)

Fig. 8. Binary image in SWD: (a) CO group; (b) CCA group; (c) CWB group; (d) WBC group.

Table 7
Crack closure of samples cured in SWD.

Mix design	Exposure age	Total image area (pixels)	Remaining crack area (pixels)	Remaining crack area (%)
CO	0 day	2264277	37214	100.00
	28 days	2264277	25726	69.13
	42 days	2264277	20533	55.18
CCA	0 day	2264277	35459	100.00
	28 days	2264277	5602	15.80
	42 days	2264277	0	0.00
CWB	0 day	2264277	45592	100.00
	28 days	2264277	5248	11.51
	42 days	2264277	178	0.39
WBC	0 day	2264277	40051	100.00
	28 days	2264277	31182	77.86
	42 days	2264277	25830	64.49

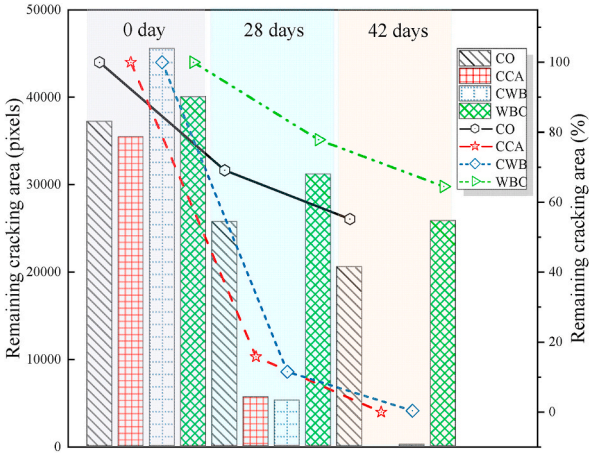

Fig. 9. Time-dependent crack closure in sodium sulphate solution.

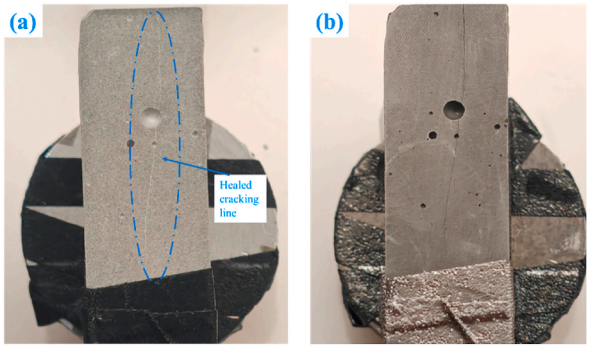

Fig. 10. SEM sample preparation: (a) original healed CCA sample; (b) Iridium coating.

were observed (Fig. 11a). Based on the map scan result at location A (Fig. 11d and e), it could be confirmed that the main healing products of samples exposed to seawater at 42 days were calcite, while small amounts of magnesium-based products and C-S-H gel were observed (Fig. 11d). Similarly, Xue et al. [24] reported the presences of magnesium hydroxide in the healing products of pre-crack sample exposed to a marine environment. Based on the mapping results (Fig. 11e), the percentages of chloride, sulphate, sodium, and potassium ions could be ignored. For Line scan at location B, the results in Fig. 11f suggested that the majority of healing products was calcite and C-S-H gel. It was evident that Ca/Si ratios between location 15 μm–20 μm were in the range of 1.1–1.4 (Fig. 11f), indicating the possible formation of C-S-H gel. However, Fig. 11g revealed very small amounts of Friedel's salt (Fs), ettringite (AFt), and brucite at 10 μm, 25 μm and 15 μm from the left end of the scanning line respectively. Han et al. [58] also observed

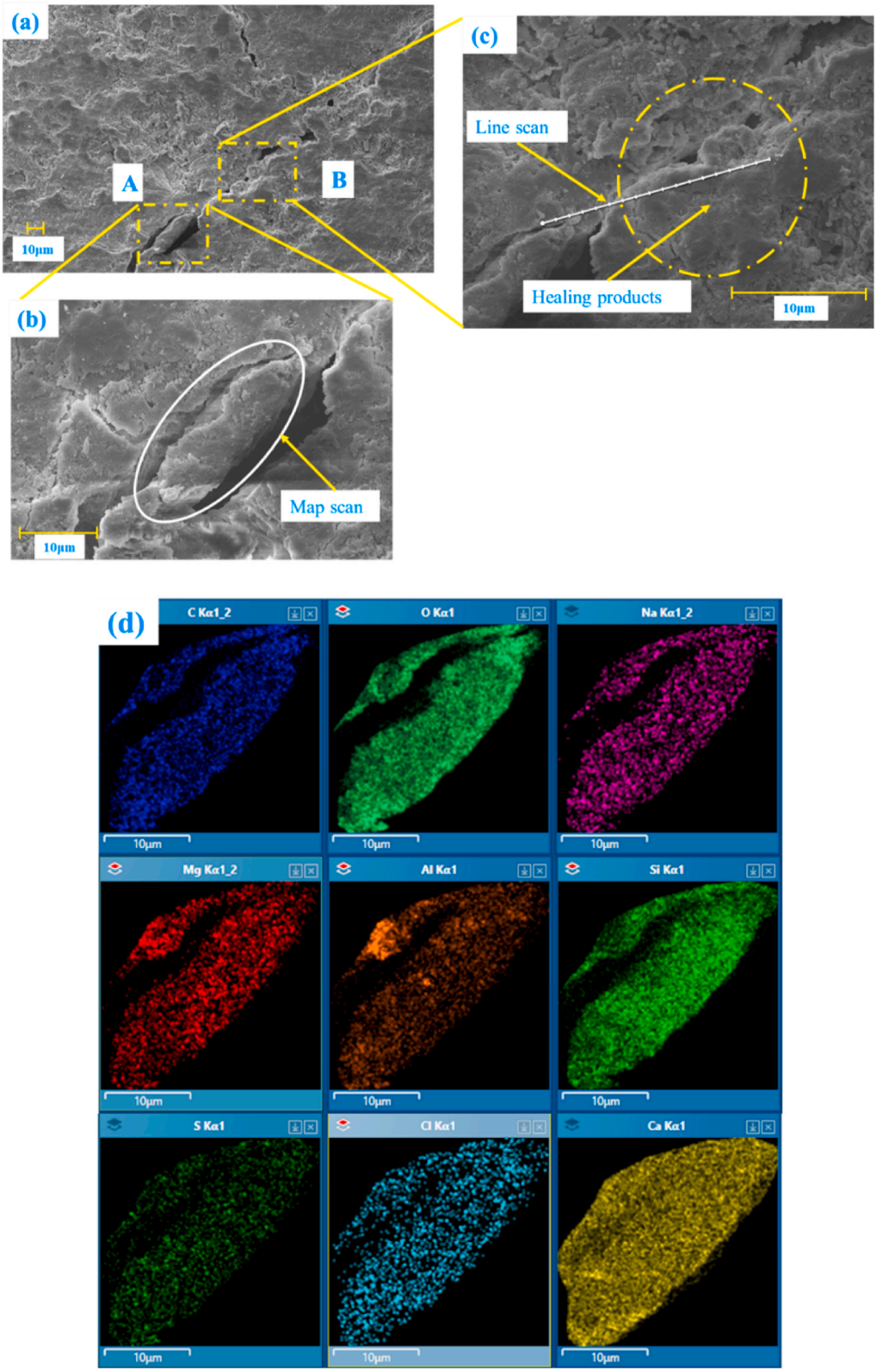

Fig. 11. Healed CCA in SWWD at 42 days: (a) ITZ in healed zone of CCA sample; (b) Map scan of location A; (c) Line scan of location B; (d) Elemental distribution in mapping; (e) EDS result of map scan; (f) Line scan result; (g) Elemental weight along select line.

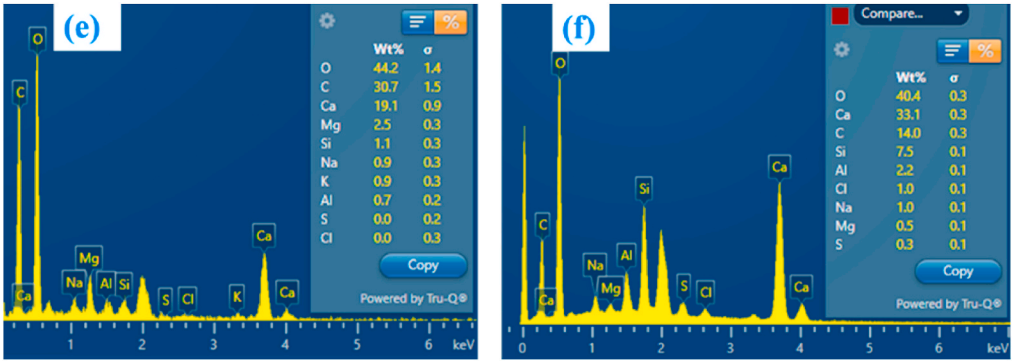

Fig. 11. (*continued*).

the formation of small content AFt in the healing products. Overall, unlike water curing where only calcite, portlandite or C-S-H gel were observed [15,59], small portions of Fs, AFt and brucite seemed to assist with the crack closure in seawater. However, EDS results could be only used as reference. The characterisations of the healing products exposed to SWWD will be discussed in the following section.

Fig. 12 depicts the ITZ analysis in a CWB sample exposed to SWD at 42 days. Using 500x magnification, point scan results at point 1 (Figs. 12d) and 2 (Fig. 12e) could classified the healing products as calcite and carbonated C-S-H gel, where the Ca/Si ratios were calculated as 7.87 and 2.42 respectively. Healing product at point 3 (Fig. 12f) could be considered as formation of Aft. In terms of point 4 (Fig. 12g), carbonated C-S-H gel seemed to form with small portion of ettringite due to the exposure to 5 % sodium sulphate solution. In order to confirm the formation of AFt in the healed zone, 5000x magnification was used in SEM-EDS. Due to the magnification increase, needle-like crystals were observed in location D in the healing product of CWB sample. EDS mapping confirmed the needle-like crystals were mainly AFt (Fig. 12h and i). It could be interpreted that AFt may be formed during the SWD assisting the healing process of CWB sample up to 42 days.

Overall, based on the SEM-EDS results, the main healing products were calcite and carbonated C-S-H gel filling the crack for both SWWD and SWD. However, limited portion of Fs and AFt may form in healing products of samples exposed to SWWD, while AFt may form in healing products of samples cured in SWD.

3.4. *Self-healing product characterisations*

Due to limited healing products on the cracking surface of CO and WBC group in all exposure conditions (Fig. 6a7, Fig. 6d7, Fig. 8a7, and Fig. 8d7), original cementitious matrix may be scratched together with the healing products, negatively impacting on the self-healing product characterisations. As a result, this study only conducted analysis on samples with complete crack closure, such as CCA and CWB group, after 42 days.

3.4.1. *XRD*

Fig. 13 compares the XRD diffraction results of self-healing products exposed to SWWD and SWD after 42 days. Since the main pattens of XRD were presented up to 60° 2θ, XRD results between 60° 2θ to 70° 2θ were not included. As shown in Fig. 13, the main component of healing products exposed to SWWD was calcite with a major peak at 29.33° 2θ, being consistent with many studies [23,24,47,51]. In terms of SWD, calcite (29.33° 2θ) was also the main healing products. Addition to the main peak, the patten of calcite could be found at peaks of 23.01°, 35.88°, 39.32°, and 43.08° 2θ. Similar peaks were also reported by Fu et al. [51]. It should be noted that the formation of calcite was affected by the solution variances and CWB addition. The XRD pattens of the four groups showed a good agreement with the aforementioned SEM-EDS results.

Notably, small peaks of portlandite and C-S-H gel were observed. According to some studies [23,47], diffraction peak at 18.3° 2θ could be interpreted either as brucite or portlandite. As a result, B/P was donated for peak at 18.3° 2θ. However, due to the supply of magnesium ions in simulated seawater, additional formation of brucite was only found in peak at 50. 93° 2θ (red and blue line in Fig. 13) for SWWD, having a good agreement with a study by Li et al. [44]. The observation of brucite in XRD also was consistent with the EDS line scan (Fig. 11g). Other peaks including 27.2°, 46.5°, and 47.5° 2θ were classified as portlandite, indicating small portions of portlandite in the healing products exposed SWWD and SWD. The XRD diffraction peaks at 26.5°, and 37.8° 2θ were attributed to C-S-H gels. However, when compared to the XRD peaks of portlandite, the peaks of C-S-H gels were relatively low, indicating less formation of C-S-H gels. In terms of AFt, self-healing products in SWD had slightly higher peaks at 9° 2θ and 15.7° 2θ than those in SWWD. Similar peaks of AFt were also reported by Refs. [23,44] in marine environment.

Overall, the XRD diffraction pattens indicated that calcite was the major healing products of pastes subjected to SWWD and SWD, while small portion of portlandite and limited amount of C-S-H gel were also found. Due to sufficient magnesium supply in simulated seawater, small amount of brucite was observed in CCA-SW and CWB-SW (Fig. 13). Healing products in SWD had slightly higher portion of AFt than those in SWWD.

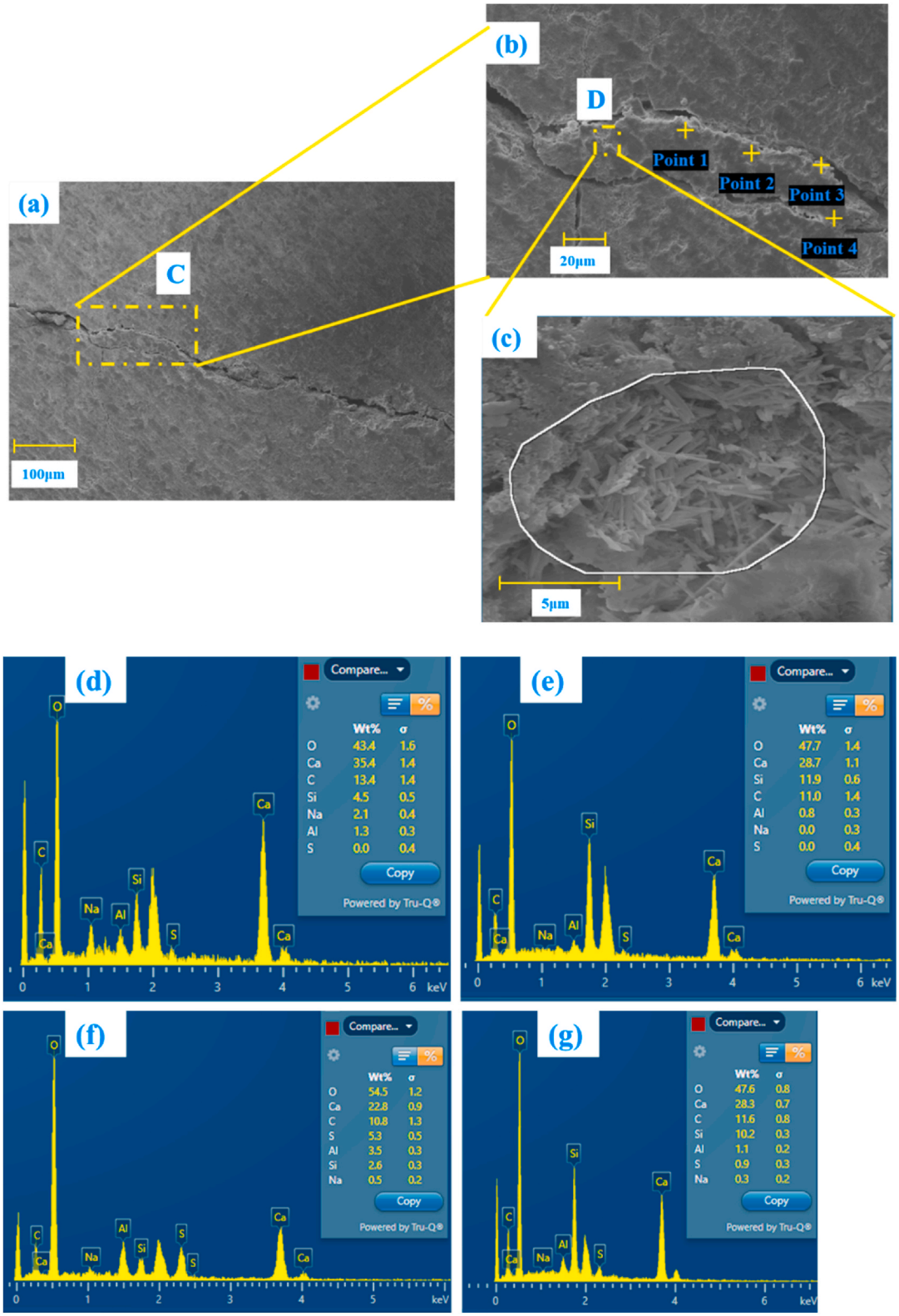

Fig. 12. CWB sample in SWD at 42 days: (a) ITZ analysis in CWB; (b) Self-healing product analysis at location C; (c) Map scan at location D; (d) Point scan result of point 1; (e) Point scan result of point 2; (f) Point scan result of point 3; (g) point scan result of point 4; (h) Mapping result at location D; (i) Elemental distribution of map scan at location D.

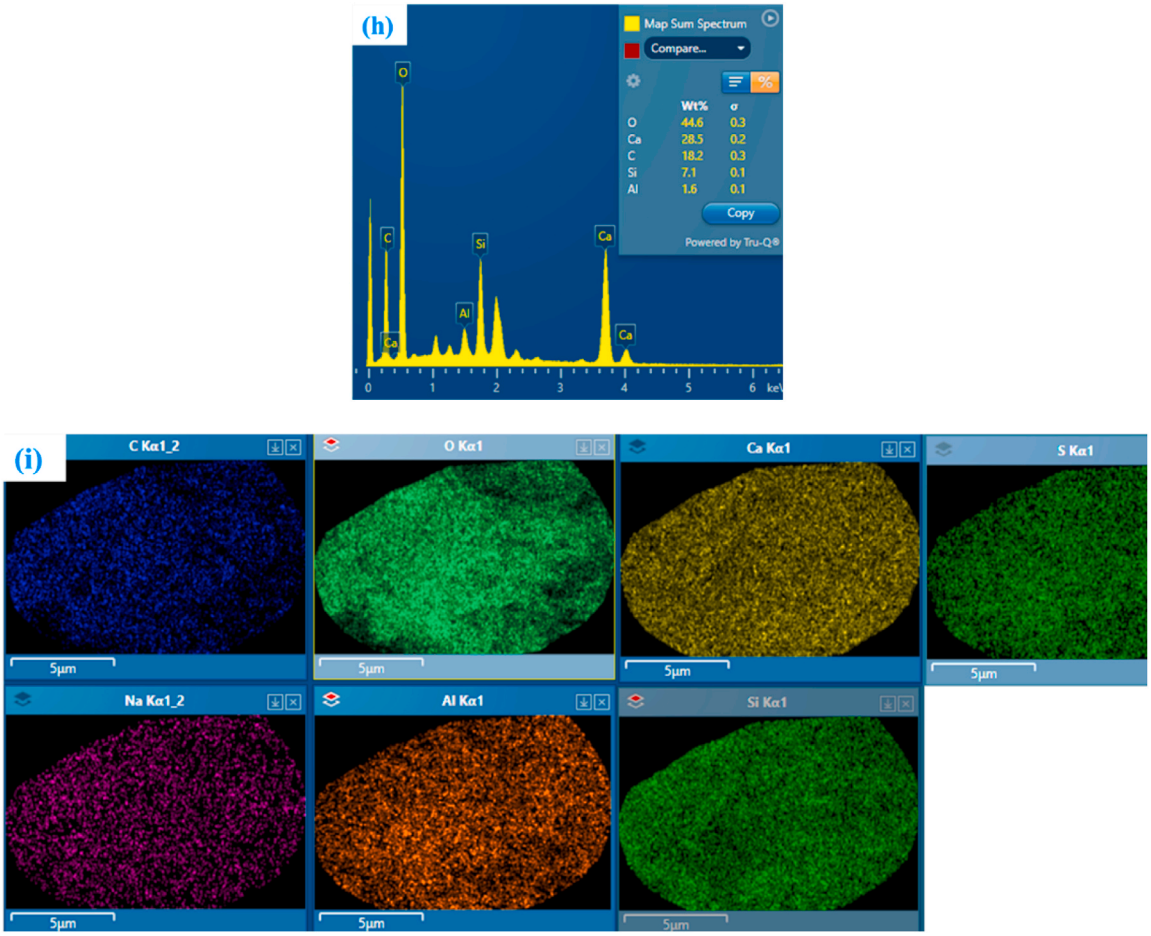

Fig. 12. (*continued*).

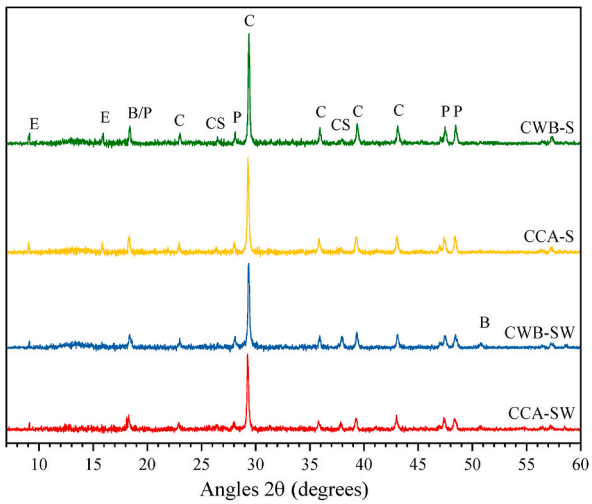

Fig. 13. XRD diffraction results of self-healing products exposed to SWWD and SWD.
(Note[1]: B = brucite; C=Calcite, CS=C-S-H gel, E = Ettringite (AFt), P=Portlandite).
(Note[2]: CCA-SW=CCA group in SWWD, CWB-SW=CWB group in SWWD, CCA-S=CCA in SWD, and CWB-S=CWB in SWD).

3.4.2. TG-DTG

Self-healing product quantifications in SWWD and SWD at 42 days were conducted using up to 30 mg powder in TG/DTG analysis. As given in Fig. 14, the first thermal event at DTG curve ranging from 60 to 200 °C was mainly attributed to the dehydration of mineral phases including C-S-H gel and Aft [47,60]. Based on many studies [24,34,41], it was difficult to precisely determine the mass loss of C-S-H gels and AFt using TG/DTG. As a result, this study only considered mass loss of φ_{other} indicating the total mass loss during the first endothermic peak within the temperature of 60–200 °C. Furthermore, it could be noted that there were small DTG peaks (in red and blue lines) in the temperature between 350 and 400 °C (Fig. 14), which was mainly due to the decomposition of brucite [23,24], while no peak was observed for healing products in SWD at this temperature rang (orange and green line). Another two distinct peaks at temperature range of 400–500 °C and 600 to 800 °C were due to the decomposition of portlandite [24,34,50] and decarbonation of calcite [12,44,47,51] respectively. All four groups had similar DTG peak at 400 to 500 °C, while there were slight differences in endothermal peak for calcite. Healing product in SWWD showed lowest peak around 743.6 °C, while a delay of the thermal peak was observed in the healing products in SWD, being 758.78 °C. This delay indicated that calcite was formed with different density in seawater and sulphate solution.

Eq. (1) and Eq. (2) were used to quantitatively determine the mass percentage of portlandite and calcite, namely $\varphi_{portlandite}$ % and $\varphi_{calcite}$ % respectively. Meanwhile, mass percentage of brucite was calculated as $\varphi_{brucite}$ % using Eq. (3).

$$\varphi_{portlandite}\,\% = (ML_{400} - ML_{500}) \times \frac{78}{18} \tag{1}$$

$$\varphi_{calcite}\,\% = (ML_{600} - ML_{800}) \times \frac{100}{44} \tag{2}$$

$$\varphi_{brucite}\,\% = (ML_{350} - ML_{400}) \times \frac{58.3}{18} \tag{3}$$

Where ML_{350}, M_{400}, M_{500}, M_{600}, and M_{800} are the mass loss percentages in the TG curve respectively. 78, 18, 100, 44, and 58.3 are the molar mass of portlandite, water, calcite, carbon dioxide, and brucite respectively.

Fig. 15 depicts the mass loss percentage of mineral phases in the different healing products using TG results. The highest portion was calcite for all four groups, which was 51.92 %, 55.65 %, 58.83 %, and 64.10 % for CCA-SW, CWB-SW, CCA-S, and CWB-S respectively. While curing pre-cracked samples in seawater, Wang only found 44 % calcite in the healing product at 42 days. The primary reason is due to insufficient calcium supply due to 30 wt% cement replacement by fly ash and GGBFS. Nevertheless, WWB addition seemed to improve the formation of calcite, where the highest calcite portion was found in CWB, being 64.1 %. Due to difficulty in quantitatively calculate the mass percentage of C-S-H gels and AFt, this study did not compare their mass. They were indicated in the φ_{other}. However, EDS results and XRD diffraction results revealed the presence of these two phases in the healing products. Small brucite portion was found approximately 3.44 % and 2.54 % in CCA-SW and CWB-SW respectively, confirming the observation of brucite in line scale and XRD pattens. In terms of portlandite, higher portions were observed in samples cured in SWWD, being 17.2 % (CCA-SW) and 15.56 % (CWB-SW) respectively, while 9.94 % and 11.24 % were found for CCA-S and CWB-S respectively.

3.4.3. FTIR

Fig. 16 shows the FTIR spectra of the healing products in SWWD and SWD. It could be found that there were three distinct peaks at 711 cm^{-1}, 872 cm^{-1} and 1407 cm^{-1} being considered as C-O band for carbonated ion [23,47]. As a result, these peaks were linked to the formation of calcite in the healing products, being in a good agreement with the aforementioned microstructural analysis. Xue et al. [23] noted that Si-O band varied in the range of 960 cm^{-1} to 1000 cm^{-1} due to carbonation of C-S-H gels. As a result, small peaks at 963 cm^{-1} and 990 cm^{-1} were classified as Si-O band, indicating small portion of C-S-H gel in the healing products. Furthermore, spectra peak at 1645 cm^{-1} and 3693 cm^{-1} were attributed to H-O band, indicating the formation of portlandite. It is worth noting that, although simulated seawater and sulphate solution were used as curing environments, no significant differences were observed for C-O, Si-O, and H-O bands. However, due to the continuous supply of sulphate ions, small portions of AFt were observed at peaks of 1076 cm^{-1} and 1110 cm^{-1}. As shown in Fig. 16, orange line and green line had relatively higher spectra signal than those of healing products in SWWD, being consistent with XRD pattens.

4. Discussions

4.1. Effects of seawater

The time-dependent healing performance of a CWB sample exposed to seawater is shown in Fig. 17. Initially, the crack width was measured as 141.56 μm using a Carl Zeiss Axiotech Vario 100 HD equipped with Eakins 48 MP FHD Camera (Fig. 5d3). Due to the random distribution of the WWB particles in the cementitious matrix, the development of the cracking path was interfered, leading to a relatively tortuous cracking surface (Fig. 17a). Exposing to seawater at 0 day, chloride, sulphate, and magnesium ions started to accumulate on the crack surface.

As shown in Fig. 17b, the crack in CWB was healed by approximately 82.01 % at 28 days (Fig. 7). It could be noted that the formation of healing products was randomly distributed along the cracking surface (Fig. 6c4), while the healing products formed on the two faces of wider crack, reducing the overall cracking area at 28 days. After 6 WD cycles in seawater, the crack was completely

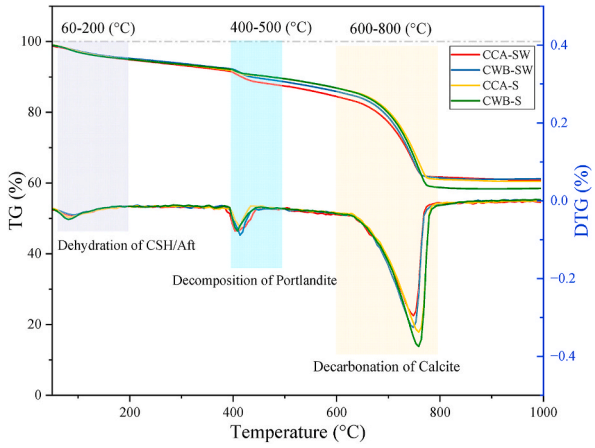

Fig. 14. TG-DTG analysis: (a) samples cured in seawater; (b) samples cured in sulphate solution.
(Note: CCA-SW=CCA group in SWWD, CWB-SW=CWB group in SWWD, CCA-S=CCA in SWD, and CWB-S=CWB in SWD).

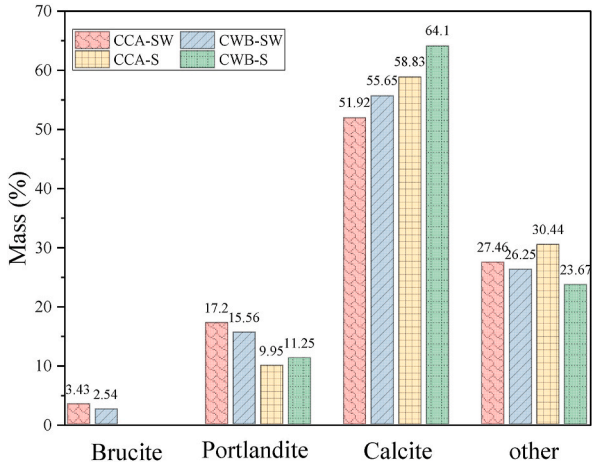

Fig. 15. Mineral phases quantification.
(Note: CCA-SW=CCA group in SWWD, CWB-SW=CWB group in SWWD, CCA-S=CCA in SWD, and CWB-S=CWB in SWD).

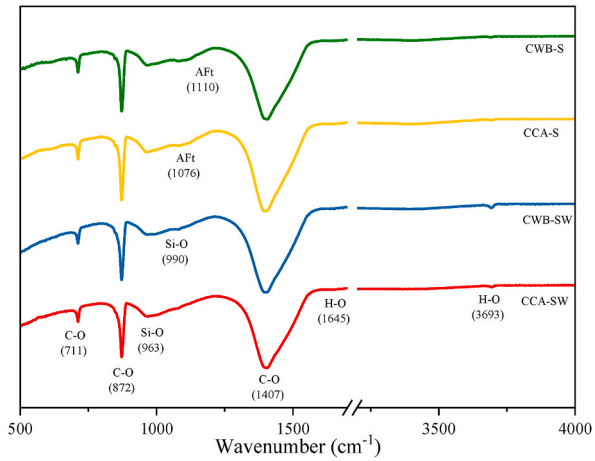

Fig. 16. FTIR spectra analysis.

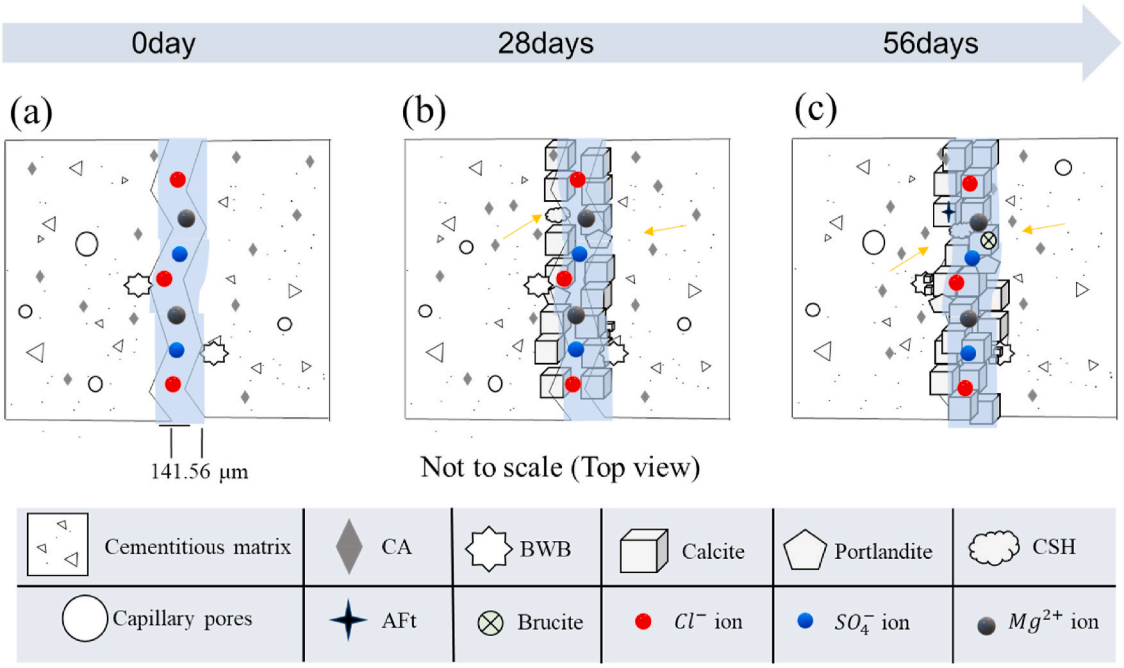

Fig. 17. Schematic diagram of self-healing process in SWWD.

healed in the CWB sample (Fig. 17c), filled by white deposits (Fig. 5d7). The EDS mapping (Fig. 11d and e) suggested that the majority of the healing products could be recognised as calcite and carbonated C-S-H gel. Based on EDS results in Fig. 11f and g, small portions of AFt and brucite might have formed, promoting the healing efficiency. XRD and TG results confirmed that the healing products in SWWD included small portion of C-S-H gel, brucite, portlandite, and large portion of calcite. 55.65 % calcite, 15.56 % portlandite, and 2.54 % brucite were found in TG analysis (Fig. 15). Furthermore, XRD pattens and FTIR spectra revealed the formation of C-S-H gel and AFt in the healing products, while the quantitative mass calculation was not conducted in the TG analysis due to difficulty in separating the mass loss of C-S-H gel and Aft at the first thermal event up to 200 °C.

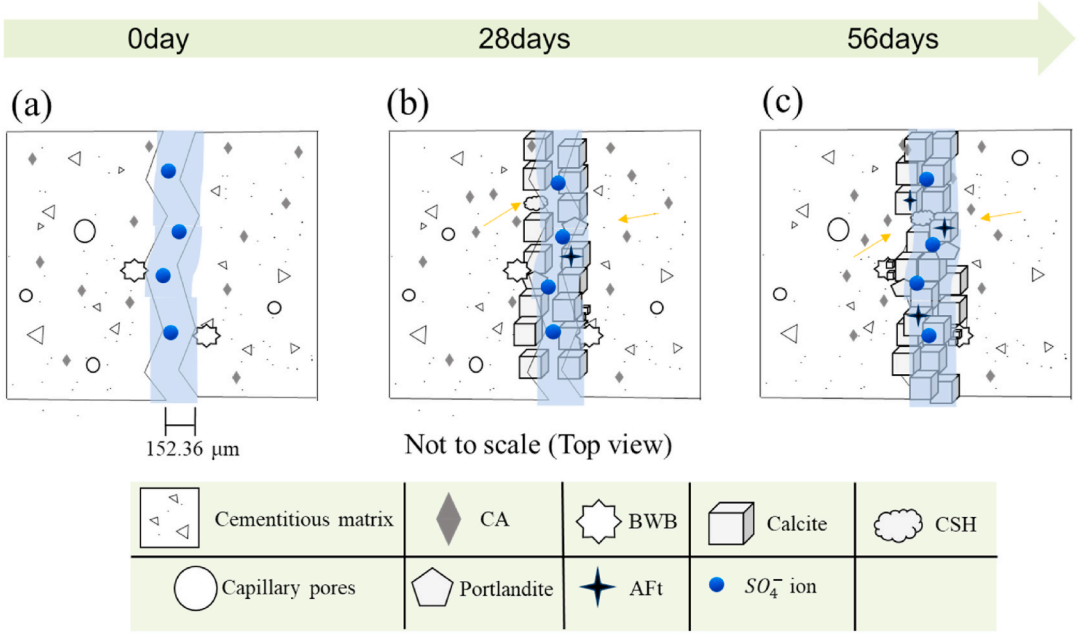

Fig. 18. Schematic diagram of self-healing process in SWD.

4.2. Effects of sulphates

In terms of CWB sample in SWD, an initial crack of 152.36 μm was measured at 0 day (Fig. 5c3), and a complex cracking path was observed in Fig. 8c1. When exposed to the 5 % sodium sulphate solution, sulphate ions accumulated on the cracking surface (Fig. 18). At 28 days, a healing rate of 88.49 % was found in binary analysis (Fig. 9), while white deposits formed at both sides of the cracked surface (Fig. 8c4). However, due to the presence of an air bubble at the top right corner of the cracking line, healing around the air bubble was negatively affected. It could be noted that although most of the cracking area were sealed at 42 days, 0.39 % unhealed cracking area remained. However, if removing the air bubble, CWB would had 100 % crack closure in SWD at 42 days.

In addition to the formation of calcite and carbonated C-S-H gel observed in SWD (Fig. 12b), EDS mapping revealed the possible formation of AFt (Fig. 12c). XRD pattens and FTIR spectra confirmed the formation of AFt. In terms of TG/DTG analysis, 64.1 % calcite and 11.24 % portlandite was calculated, indicating that the main components in healing products were calcium-based phases. Similar to SWWD, the mass percentage of C-S-H gel and AFt could not be included in healing products characterisation in SWD.

Overall, by comparing the healing behaviour of samples in SWWD and SWD, it appears that: WWB significantly interferes with the formation of the cracking line due to weak ITZ between WWB and the cementitious matrix. It is evident from the binary analysis in Fig. 6c1 and Fig. 8c1. Tortuous cracking path allows more sites for healing products, promoting the healing behaviours of WWB-cement composites. Although the presence of seawater and sulphate ions improve the healing performance, no significant difference are observed. Secondly, CA addition significantly improves the healing rate when comparing CWB and WBC samples in both exposure conditions.

5. Conclusion

This study investigated the healing performances of waste wood biochar-cement (WWB-cement) composites with crystalline admixture (CA) exposed to simulated seawater or sulphate solution. The self-healing rate was monitored using optical microscopy combined with binary image processing. The self-healing products were characterised using SEM-EDS, XRD, TG, and FTIR. The main findings are as follows:

- After 28 days of wet/dry cycles using simulated seawater (SWWD) solution, the cracking surface area in the 1 wt% CA specimens (CCA group) was healed up to 86.36 %. The cracking surface area in the 1 wt% CA and 5 wt% WWB specimens (CWB group) was healed up to 82.01 %. WWB did not improve self-healing. Self-healing of specimens without CA (with or without WWB) achieved only about 15–20 % of the cracking surface area after 28 days, confirming no beneficial effect of WWB. After 42 days, cracking was completely healed in all samples with CA (with or without WWB). Whereas, only about 40 % self-healing was achieved in specimens without CA.
- Similar results were obtained for wet/dry cycles exposure using sulphate (SWD) solution. After 28 days, the cracking surface area was healed up to 84.2 % and 88.49 % in the 1 wt% CA specimens (CCA group) and in the 1 wt% CA and 5 wt% WWB specimens (CWB group) respectively, showing only a marginal improvement by WWB. After 42 days, cracking was also completely healed in all samples with CA (with or without WWB). Regarding the specimens without CA, self-healing reached about 45 % for the WWD-free control specimen (CO group) and about 35 % for the specimen with WWB (WBC group).
- Using 5 wt% WWB to partially replace cement, led to complex and tortuous cracking paths compared to WWB-free specimens, but WWB did not influence significantly self-healing. Only CA admixture improved greatly the self-healing performance of all cementitious composites tested.
- For SWWD exposure, EDS mapping and line scan results suggested that calcite was the main healing product. But small amounts of brucite and ettringite (AFt) were also observed. XRD and TG/DTG results confirmed the formation of calcite, portlandite, and small amounts of C-S-H gel and AFt. Furthermore, 51.92 % and 55.65 % calcite was found in CCA and CWB group respectively from TG results. 3.44 % and 2.54 % brucite was also observed for CCA and CWB respectively.
- In SWD exposure, calcite was also the main healing product. But a small amount of AFT was observed using EDS mapping and confirmed by XRD and TG results. 58.83 % and 64.10 % calcite were calculated for CCA and CWB respectively from TG results.
- In this study, although WWB addition did not improve healing performance of WWB-cement composites, it led to tortuous cracking path while absorbing more cracking energy. For future studies, there is an increasing trend of using different SCMs, such as biochar, to partially replace OPC, lowering carbon footprint and improving durability properties of concrete structures.

CRediT authorship contribution statement

Xuqun Lin: Writing – original draft, Visualization, Validation, Software, Methodology, Investigation, Formal analysis, Data curation, Conceptualization. **Quang Dieu Nguyen:** Writing – review & editing, Supervision, Resources, Project administration, Methodology, Investigation, Conceptualization. **Arnaud Castel:** Writing – review & editing, Supervision, Project administration, Investigation, Funding acquisition. **Zhizhong Deng:** Writing – review & editing, Investigation. **Wengui Li:** Writing – review & editing, Investigation. **Vivian W.Y. Tam:** Writing – review & editing, Investigation.

Declaration of competing interest

The authors declare that they have no known competing financial interests or personal relationships that could have appeared to

influence the work reported in this paper.

Acknowledgements

The authors want to highly appreciate Australian Research Council (DP220101051), Australia and the supports from University of Technology Sydney Research Academic Program at Tech Lab (UTS RAPT).

Data availability

Data will be made available on request.

References

[1] A. Sidiq, R. Gravina, F. Giustozzi, Is concrete healing really efficient? A review, Construct. Build. Mater. 205 (2019) 257–273.
[2] X. Lin, W. Li, A. Castel, T. Kim, Y. Huang, K. Wang, A comprehensive review on self-healing cementitious composites with crystalline admixtures: design, performance and application, Construct. Build. Mater. 409 (2023) 134108.
[3] P. Zhang, Y. Dai, X. Ding, C. Zhou, X. Xue, T. Zhao, Self-healing behaviour of multiple microcracks of strain hardening cementitious composites (SHCC), Construct. Build. Mater. 169 (2018) 705–715.
[4] P. Chindasiriphan, H. Yokota, P. Pimpakan, Effect of fly ash and superabsorbent polymer on concrete self-healing ability, Construct. Build. Mater. 233 (2020) 116975.
[5] N. De Belie, E. Gruyaert, A. Al-Tabbaa, P. Antonaci, C. Baera, D. Bajare, A. Darquennes, R. Davies, L. Ferrara, T. Jefferson, C. Litina, B. Miljevic, A. Otlewska, J. Ranogajec, M. Roig-Flores, K. Paine, P. Lukowski, P. Serna, J.-M. Tulliani, S. Vucetic, J. Wang, H.M. Jonkers, A review of self-healing concrete for damage management of structures, Adv. Mater. Interfac. 5 (17) (2018) 1800074.
[6] Y. Tian, J. Bao, W. Guo, P. Zhang, Y. Cui, T. Zhao, Autogenous self-healing of cracked concrete exposed to the marine tidal zone, Construct. Build. Mater. 357 (2022) 129336.
[7] G. Lefever, D. Van Hemelrijck, D.G. Aggelis, D. Snoeck, Evaluation of self-healing in cementitious materials with superabsorbent polymers through ultrasonic mapping, Construct. Build. Mater. 344 (2022) 128272.
[8] C. Ma, F. Fan, M. Chen, S. Li, Y. Chen, Z. Pan, R. Liu, Preparation of a novel superabsorbent fiber–cement composite and evaluation of its self-healing performance, Cement Concr. Compos. 133 (2022) 104713.
[9] J.W.C. Pang, I.P. Bond, A hollow fibre reinforced polymer composite encompassing self-healing and enhanced damage visibility, Compos. Sci. Technol. 65 (11) (2005) 1791–1799.
[10] D. Snoeck, J. Debo, N. De Belie, Translucent self-healing cementitious materials using glass fibers and superabsorbent polymers, Develop. Built Environ. 3 (2020) 100012.
[11] X. Xiao, C. Unluer, S. Chu, E.-H. Yang, Single bacteria spore encapsulation through layer-by-layer self-assembly of poly(dimethyldiallyl ammonium chloride) and silica nanoparticles for self-healing concrete, Cement Concr. Compos. 140 (2023) 105105.
[12] J. Xu, X. Wang, W. Yao, Q. Chen, H. Zhu, S.P. Shah, Understanding the formation and structure of bio-mineralization for self-healing of marine concrete: an experimental and thermodynamic approach, Cement Concr. Compos. 145 (2024) 105369.
[13] J. Feng, R.E. Binte Rohaizat, S. Qian, Unveiling the impact of graphene oxide on bacteria-based autonomous healing of cracks in cementitious composites, Cement Concr. Compos. 151 (2024) 105596.
[14] X. Wang, J. Xu, Z. Wang, W. Yao, Use of recycled concrete aggregates as carriers for self-healing of concrete cracks by bacteria with high urease activity, Construct. Build. Mater. 337 (2022) 127581.
[15] C. Zhang, R. Lu, Y. Li, X. Guan, Effect of crystalline admixtures on mechanical, self-healing and transport properties of engineered cementitious composite, Cement Concr. Compos. 124 (2021) 104256.
[16] T.S.R. Chandra, A. Ravitheja, Macro mechanical properties of self healing concrete with crystalline admixture under different environments, Ain Shams Eng. J. 10 (1) (2019) 23–32.
[17] B. Park, Y.C. Choi, Effect of healing products on the self-healing performance of cementitious materials with crystalline admixtures, Construct. Build. Mater. 270 (2021) 121389.
[18] R. Flores, M, S. Moscato, P. Serna, L. Ferrara, Self-healing capability of concrete with crystalline admixtures in different environments, Construct. Build. Mater. 86 (2015) 1–11.
[19] C.M. Tibbetts, K.A. Riding, C.C. Ferraro, A critical review of the testing and benefits of permeability-reducing admixtures for use in concrete, Cement 6 (2021) 100016.
[20] L. Ferrara, V. Krelani, M. Carsana, A "fracture testing" based approach to assess crack healing of concrete with and without crystalline admixtures, Construct. Build. Mater. 68 (2014) 535–551.
[21] X. Hu, J. Xiao, Z. Zhang, C. Wang, C. Long, L. Dai, Effects of CCCW on properties of cement-based materials: a review, J. Build. Eng. 50 (2022) 104184.
[22] G.S. Munhoz, M.E.G. Dobrovolski, E. Pereira, R.A. Medeiros-Junior, Effect of improved autogenous mortar self-healing in the alkali-aggregate reaction, Cement Concr. Compos. 117 (2021) 103905.
[23] C. Xue, W. Li, Z. Luo, K. Wang, A. Castel, Effect of chloride ingress on self-healing recovery of smart cementitious composite incorporating crystalline admixture and MgO expansive agent, Cement Concr. Res. 139 (2021) 106252.
[24] C. Xue, Performance and mechanisms of stimulated self-healing in cement-based composites exposed to saline environments, Cement Concr. Compos. 129 (2022) 104470.
[25] E. Cuenca, A. Mezzena, L. Ferrara, Synergy between crystalline admixtures and nano-constituents in enhancing autogenous healing capacity of cementitious composites under cracking and healing cycles in aggressive waters, Construct. Build. Mater. 266 (2021) 121447.
[26] C. Xue, W. Li, F. Qu, Z. Sun, S.P. Shah, Self-healing efficiency and crack closure of smart cementitious composite with crystalline admixture and structural polyurethane, Construct. Build. Mater. 260 (2020) 119955.
[27] P. Azarsa, R. Gupta, A. Biparva, Assessment of self-healing and durability parameters of concretes incorporating crystalline admixtures and Portland Limestone Cement, Cement Concr. Compos. 99 (2019) 17–31.
[28] E. Cuenca, A. Tejedor, L. Ferrara, A methodology to assess crack-sealing effectiveness of crystalline admixtures under repeated cracking-healing cycles, Construct. Build. Mater. 179 (2018) 619–632.
[29] K.S. Lauch, J.P. Charron, C. Desmettre, Comprehensive evaluation of self-healing of concrete with different admixtures under laboratory and long-term outdoor expositions, J. Build. Eng. 54 (2022) 104661.
[30] E. Tsampali, M. Stefanidou, The role of crystalline admixtures in the long-term healing process of fiber-reinforced cementitious composites (FRCC), J. Build. Eng. 60 (2022) 105164.
[31] L. Ferrara, V. Krelani, F. Moretti, On the use of crystalline admixtures in cement based construction materials: from porosity reducers to promoters of self healing, Smart Mater. Struct. 25 (8) (2016) 084002.
[32] G. Li, S. Liu, M. Niu, Q. Liu, X. Yang, M. Deng, Effect of granulated blast furnace slag on the self-healing capability of mortar incorporating crystalline admixture, Construct. Build. Mater. 239 (2020) 117818.

[33] K. Aspiotis, K. Sotiriadis, A. Ntaska, P. Mácová, E. Badogiannis, S. Tsivilis, Durability assessment of self-healing in ordinary Portland cement concrete containing chemical additives, Construct. Build. Mater. 305 (2021) 124754.
[34] C. Xue, Cracking and autogenous self-healing on the performance of fiber-reinforced MgO-cement composites in seawater and NaCl solutions, Construct. Build. Mater. 326 (2022) 126870.
[35] M.Z.Y. Ting, K.S. Wong, M.E. Rahman, S.J. Meheron, Deterioration of marine concrete exposed to wetting-drying action, J. Clean. Prod. 278 (2021) 123383.
[36] R. Yin, B. Li, C. Zhang, Q. Wu, H. Xie, Y. Wang, The permeability of SO42− and Cl− in concrete under the effect of seepage flow and stress fields, Construct. Build. Mater. 162 (2018) 697–703.
[37] S. Lu, P. Zhao, C. Liang, L. Liu, Z. Qin, S. Wang, P. Hou, L. Lu, Utilization of Polydimethylsiloxane (PDMS) in polymer cement-based coating to improve marine environment service performance, Construct. Build. Mater. 367 (2023) 130359.
[38] M.Z.Y. Ting, X. Sun, Y. Yi, Seawater resistance of blastfurnace slag activated by reactive magnesia with different reactivities: durability performance and deterioration mechanism, Construct. Build. Mater. 444 (2024) 137832.
[39] B. Zhang, F. Xu, H. Zhu, Z. Yang, H. Peng, Deterioration of bond performance between BFRP bars and coral aggregate concrete incorporating slag-based geopolymers under seawater corrosion environments, Construct. Build. Mater. 411 (2024) 134518.
[40] W. Xu, Y. Zhang, M. Li, F. Qu, C.S. Poon, X. Zhu, D.C.W. Tsang, Durability and micromechanical properties of biochar in biochar-cement composites under marine environment, J. Clean. Prod. 450 (2024) 141842.
[41] F. Qu, Y. Zhang, X. Zhu, W. Xu, C.S. Poon, W. Li, D.C.W. Tsang, Roles of wood waste biochar for chloride immobilization in GGBS-blended cement composites, Construct. Build. Mater. 411 (2024) 134389.
[42] X. Lin, W. Li, Y. Guo, W. Dong, A. Castel, K. Wang, Biochar-cement concrete toward decarbonisation and sustainability for construction: characteristic, performance and perspective, J. Clean. Prod. 419 (2023) 138219.
[43] X. Lin, A. Castel, Z. Deng, B. Dong, X. Zhang, S. Zhang, W. Li, Effect of crystalline admixtures on shrinkage and alkali-silica reaction of biochar-cementitious composites, Develop. Built Environ. 18 (2024) 100456.
[44] P. Li, W. Li, K. Wang, J.L. Zhou, A. Castel, S. Zhang, S.P. Shah, Hydration of Portland cement with seawater toward concrete sustainability: phase evolution and thermodynamic modelling, Cement Concr. Compos. 138 (2023) 105007.
[45] Z. Lu, Y. Li, J. Xie, Durability of BFRP bars wrapped in seawater sea sand concrete, Compos. Struct. 255 (2021) 112935.
[46] A. International, ASTM D1141-98: Standard Practice for Preparation of Substitute Ocean Water, 2021.
[47] R. Wang, Z. Ding, Y. Zhang, Y. Xu, Self-healing of high-performance engineered cementitious materials with crystalline admixture in the seawater environment, J. Build. Eng. 63 (2023) 105472.
[48] L. Ferrara, T. Van Mullem, M.C. Alonso, P. Antonaci, R.P. Borg, E. Cuenca, A. Jefferson, P.-L. Ng, A. Peled, M. Roig-Flores, M. Sanchez, C. Schroefl, P. Serna, D. Snoeck, J.M. Tulliani, N. De Belie, Experimental characterization of the self-healing capacity of cement based materials and its effects on the material performance: a state of the art report by COST Action SARCOS WG2, Construct. Build. Mater. 167 (2018) 115–142.
[49] J. Li, X. Guan, Pretreated lightweight aggregates for self-healing concrete exposed to calcium hydroxide-rich sewage, Construct. Build. Mater. 365 (2023) 130117.
[50] P. Zhan, J. Wang, H. Zhao, W. Li, S.P. Shah, J. Xu, Impact of synthetic C-S-H seeds on early hydration and pore structure evolution of cement pastes: a study by 1H low-field NMR and path analysis, Cement Concr. Res. 175 (2024) 107376.
[51] Q. Fu, S. Zhang, J. Zhou, J. Wang, X. Wang, Q. Huang, L. Lu, The synergistic effect of microorganisms and multiple admixtures on improving the self-healing of cracks in biogenic mortar exposed to different marine environments, Construct. Build. Mater. 423 (2024) 135884.
[52] K. Van Tittelboom, E. Gruyaert, H. Rahier, N. De Belie, Influence of mix composition on the extent of autogenous crack healing by continued hydration or calcium carbonate formation, Construct. Build. Mater. 37 (2012) 349–359.
[53] L. Restuccia, G.A. Ferro, Promising low cost carbon-based materials to improve strength and toughness in cement composites, Construct. Build. Mater. 126 (2016) 1034–1043.
[54] S. Gupta, H.W. Kua, C.Y. Low, Use of biochar as carbon sequestering additive in cement mortar, Cement Concr. Compos. 87 (2018) 110–129.
[55] Y.-z. Zhang, L.-y. Liu, G. Wei, L.-y. Lai, Investigating the self-healing performance of cracked undersea constructions, J. Build. Eng. 80 (2023) 107928.
[56] P. He, J. Yu, R. Wang, W. Du, X. Han, S. Gu, Q. Liu, Effect of ion chelator on pore structure, mechanical property and self-healing capability of seawater exposed mortar, Construct. Build. Mater. 246 (2020) 118480.
[57] H. Liu, H. Huang, X. Wu, H. Peng, Z. Li, J. Hu, Q. Yu, Effects of external multi-ions and wet-dry cycles in a marine environment on autogenous self-healing of cracks in cement paste, Cement Concr. Res. 120 (2019) 198–206.
[58] C. Han, W. Shen, X. Ji, Z. Wang, Q. Ding, G. Xu, Z. Lv, X. Tang, Behavior of high performance concrete pastes with different mineral admixtures in simulated seawater environment, Construct. Build. Mater. 187 (2018) 426–438.
[59] W. Tian, Y. Liu, W. Wang, Multi-structural evolution of conductive reactive powder concrete manufactured by enhanced ohmic heating curing, Cement Concr. Compos. 123 (2021) 104199.
[60] Z. Tang, B. Cao, C. Litina, V. Afroughsabet, C. Vlachakis, A. Al-Tabbaa, Development of novel self-healing strain-hardening cementitious composites (SH2CC) for dynamic cyclic loading conditions using mineral and polymer admixtures, Cement Concr. Compos. 142 (2023) 105172.